NORTHWESTERN UNIVERSITY

X-ray Reflectivity Study of Ionic Liquids at Electrified Surfaces

A DISSERTATION

SUBMITTED TO THE GRADUATE SCHOOL

IN PARTIAL FULFILLMENT OF THE REQUIREMENTS

for the degree

DOCTOR OF PHILOSOPHY

Field of Physics

By

Miaoqi Chu

EVANSTON, ILLINOIS

March 2017

ABSTRACT

X-ray Reflectivity Study of Ionic Liquids at Electrified Surfaces

Miaoqi Chu

Room temperature ionic liquids (RTILs) are molten salts at room temperature, consisting purely of anions and cations, with many potential applications in energy storage, electrosynthesis, electrodeposition, green chemistry etc. The solvent-free and highly charge-concentrated novel liquids possess many unique properties that are not seen in conventional dilute electrolyte solutions. Among them, the structures and dynamics of anions/cations next to charged surfaces are especially important because of their direct relevance to energy applications. Numerous theoretical studies based on mean-field theory and computer simulations predict that when a surface is not highly charged, RTILs form alternating layers of anions/cations to screen the surface charge; when it is highly charged, a crowded layer of ions with like charge forms. The alternating anion/cation layer structure has been observed experimentally, but not the crowding effect.

In this thesis, studies of the interfacial structures and dynamics of RTILs with synchrotron based specular X-ray reflectivity (XRR), a non-contact, non-destructive probe of structure, are described. This powerful technique measures the electron density profile

at the interface, from which one can infer the molecular ordering of anions/cations. In-situ XRR is measured on a conductive silicon substrate, which also serves as the working electrode, in a transmission cell filled with RTIL. The selection of experimental material and the design of the cell, made it possible to directly observe the crowding of anions.

At low voltages, the XRR curve is featureless, indicating that the interfacial structure (if any) is too thin to be detected. Above a certain threshold voltage, fringes develop in XRR scans, which are due to the electron-dense anions aggregating at the silicon surface, or in other words the crowding effect. The thickness of this layer is found to be proportional to the square root of the voltage minus an offset voltage. The origin of the offset, which is not predicted in theories, may be due to an alternating layer or a diffuse Gouy-Chapman double layer. The composition of the crowded layer is roughly 80% anions and 20% cations, while theories predicate 100% anion. Furthermore, the charge carried by each anion/cation is less than unit charge, in agreement with the predictions of quantum-chemical calculation.

By measuring the time dependence of the crowded layer, ultraslow dynamics with timescales of 400-1100 sec. is found. This time scale is at least 5 orders longer than the RC constant, but 10 times shorter than the time needed for ions to diffuse freely across the entire electrochemical cell. These significant differences mean that the crowding cannot result from just the local reordering of anions/cations but is due a collective reorganization that happens across the whole electrochemical cell.

This thesis reveals some of the complex properties of RTILs. It provides fundamental information that may motivate and promote research and applications using RTILs.

Acknowledgements

I would like to thank Prof. Pulak Dutta for his continuous support during the past 6 years. Dr. Dutta provided me a great working environment with enormous amount of freedom, high scientific standards as well as tolerance for failure. I was encouraged to explore new frontiers and Dr. Dutta's always willing to support me both mentally, intellectually, and logistically. I cherish the years spent in his group.

This work wouldn't be possible without the group peers, past or present, in the Dutta's group. Dr. Guennadi Evmenenko generously shared his life-long knowledge of X-ray and neutron scattering setup and data analysis techniques. In addition, Guenna's unpublished work on thin-film ionic liquids inspired this research. I also benefited from Guenna's optimist attitude to life and his love for movies, food and travel. Ahmet Uysal and Benjamin Stripe helped me with my first experiment and taught me Synchrotrons 101. For the past four years, I'm especially grateful to Mitchell Miller who helped me prepare samples and worked numerous night-shifts without any complaints.

I would also like to express my thanks to the beamline scientists at Argonne National Lab, Sungsik Lee and Benjamin Reinhart at 12BM-B and Christian M. Schlepütz and Evguenia Karapetrova at 33BM-C. Their professional knowledge of the sectors as well as their willingness to customize stages and detectors to accommodate my experiments made each run enjoyable and fruitful.

None of this would have been possible without the support and encouragement from my sister and brother in law, Qingzhao Chu and Jun Wu, as well as my uncles, Senlin Chu and Xiansheng Zhu. They took good care of the family when I was 7000 miles away. Finally, I'm profoundly grateful to my father and mother, Xianglin Chu and Wanying Zhu, for their unconditional support and love. Since 1993, the year I was sent to the kindergarten, they have been persistently devoted to my education and never asked for a return. This work is dedicated to my parents.

Table of Contents

List of Tables

List of Figures

CHAPTER 1

Basics of X-ray reflectivity

1.1. Introduction

X-ray reflectivity (XRR) is a powerful technique that measures the electron density profile (EDP) perpendicular to the surfaces. It's widely used to characterize surface properties including thin-film structures, molecular arrangements and ion distributions. XRR was first observed by Heinz Kiessig[**1**] in 1931 and the conceptual idea was developed by Layman Parratt in 1954 [**2**]. Since then, XRR has been developed into a successful technique used in physics, chemistry, biophysics and material science, thanks to the advent of synchrotron X-ray source, advanced photon detector and developments in computer technologies. Each year, more than 250 papers and thousands of citations are attributed to XR, according to WebofScience.

As the name suggests, an XRR experiment shoots an X-ray beam onto the sample surface and measures the portion of photons that are reflected in the specular direction. If the surface is ideally sharp and without graduated electron density (structures), the reflectivity will follow the Fresnel form. Deviation from Fresnel reflectivity, on the other hand, suggests surface roughness and/or non-uniform surface layers. With proper analyzing procedure, the EDP in real space can be reconstructed from the reflectivity data. XRR can detect structures from a few angstroms to a few hundred angstroms.

Excluding the synchrotron X-ray source, the rest of experimental setup is quite straightforward. It only requires a diffractometer, a detector, and other accessories like motors and slits. The non-contact and non-destructive (let's not worry about beam-damage for now) nature makes it possible to perform XRR measurements in-situ. The samples can be measured under the desirable conditions, such as temperature, humidity, pressure, pH, electric field and magnetic field.

Every technique has its advantages and disadvantages. Unlike many spectroscopic methods, XRR is only sensitive to the electron density (electrons per unit volume). If the X-ray energy is close to the absorption edge of elements presented on the surface, resonant anomalous XRR can be employed to study the system. But this luxury isn't always available for studies with soft-matter, which largely consist of elements (C, O, H, N) with absorption edges far below the X-ray energy. Unlike neutron reflectivity (NR) in which the scattering length density (SLD) can be tuned by replacing a certain portion of hydrogen to deuterium, electron density can be considered as a constant once a sample is prepared. Nevertheless, one can optimize the electron density contrast by choosing the material/substrates wisely.

XRR only measures the electron density perpendicular to the surface (out of plane), while the details parallel to the surface (in plane) are averaged. Thus, other techniques which can characterize the in-plane structure, such as grazing incidence diffraction (GID) and small angle X-ray scattering (SAXS), are required as complementary tools to reveal the 3D structure.

Also, beam-damage effect from X-rays cannot be neglected. An intense X-ray beam ionizes the medium in its path, releasing free radicals that are highly active[**3**]. Molecules

with certain chemical structures, for example carbon double-bonds, are especially vulnerable to the free radicals[**4**]. Thus measures should be taken to mitigate the beam-damage effect. For example, take the measurement under cryogenic conditions; fill the experimental chamber with inert gas; perform beam-damage test at the beginning of the experiment; move the scan spot constantly; prepare a new sample frequently.

Due to the fast decaying nature of XRR as a function of wave vector transfer (which will be elaborated in the next section), finite photon flux (even with synchrotron sources) and slow motor control, the resolution of XRR is limited both in terms of space (a few angstroms) and time (tens to hundreds of seconds). This puts a hard limit on how small a structure and how fast a time scale XRR can distinguish, clearly not a single chemical bond or a chemical reaction that takes a femtosecond.

Finally, the reconstruction of XRR data (as well as NR data) for real space information is an inverse problem[**5**]. The X-ray detector is able to record the number of photons but not the phase. Cares must be taken in order to achieve robust and physically reasonable conclusions.

A typical XRR experiment and its data analysis process is shown in Figure 1.1. The details will be described in the next few sections. Briefly, the raw data from XRR experiment are corrected for geometry, attenuation in the X-ray path, transmission factor of filters, scan time and background, before being finally normalized by the incoming beam flux. Meantime, a method to model the EDP in real space must be developed. Several schemes are proposed, such as Fourier series/Chebyshev polynomials, distorted crystals, and slab (box) model. In this thesis, the slab model, which divides the EDP into separate

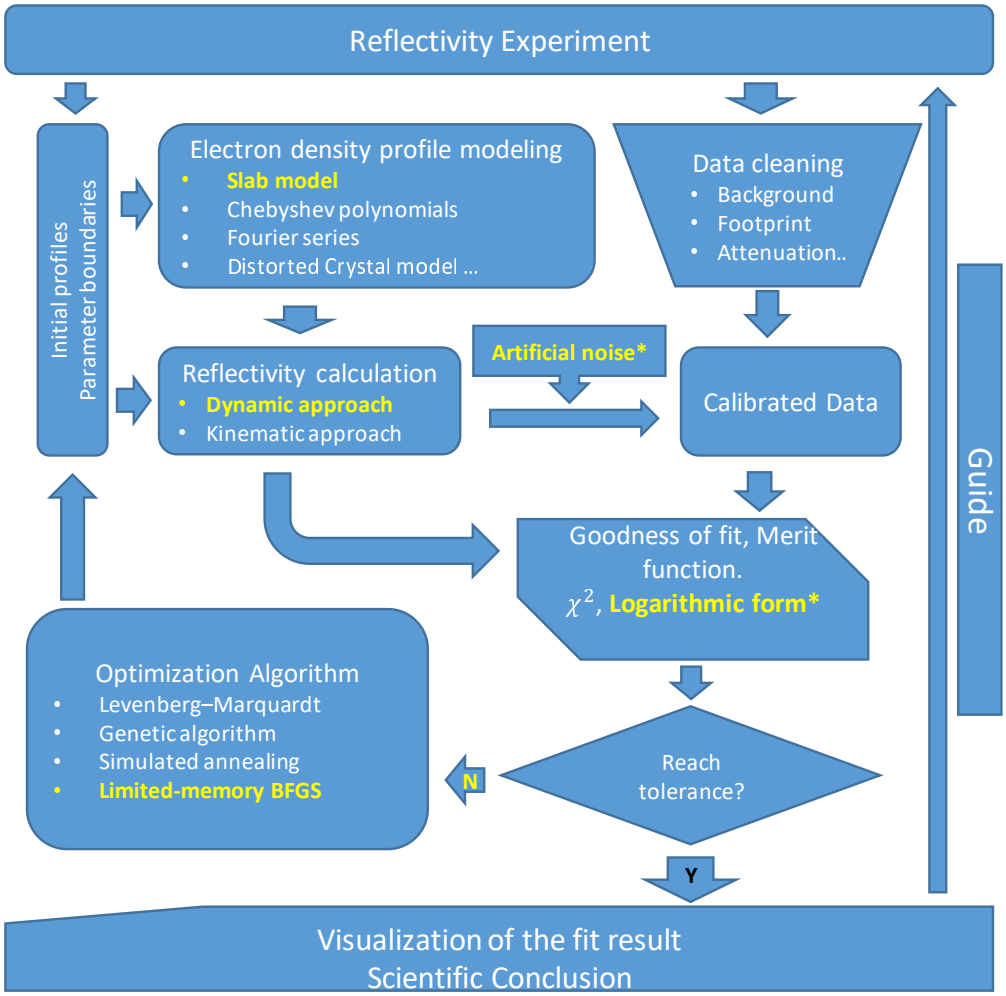

Figure 1.1. Scheme of X-ray reflectivity data analysis procedure. For each step, the highlighted option is used in this research and will be explained in details in the following sections.

slabs and characterizes the interfaces with an error function, is the primary model due to its simplicity, clear physical picture and easy Fourier conversion. From the model whose parameters (profile) are within proper boundaries imposed by physical reasonability for the real system, reflectivity curve can be calculated with different formalisms. A merit function which describes the goodness of fitting compares the experimental data to the calculated reflectivity curve. Then an optimization algorithm steps in to navigate the

profile which can have a highly non-linear merit function value though high-dimensional parametric space, until the merit function reaches the fitting tolerance (which means a satisfactory profile is found). The fitting result with error-bar and correlation between fitting variables is reported to support the scientific conclusion. In this thesis, a scheme which generates simulated reflectivity data is also proposed, which can be used to calibrate the fitting program and test experiment ideas. A systematic summary of the fitting result of reflectivity data either from experiments or from simulations, also serve as a good guide on how to design an XRR experiments that optimize the output.

1.2. Modeling the electron density profile

XRR has a finite spatial resolution limit, and electron distributions, smaller than this limit can't be distinguished. In other words, the EDP is averaged over this length scale, which is usually larger than the length of chemical bonds. Thus, the EDP should be considered as a continuous, differentiable function of z, where z is the perpendicular position. This differs from crystallography in which the distribution of atoms is treated as a superposition of delta functions.

In this thesis, the primary model is the slab model,

$$\rho(z) = \rho_0 + \sum_{i=1}^{N} \frac{\rho_i - \rho_{i-1}}{2} \left(erf(\frac{z - h_i}{\sqrt{2}\sigma_i}) + 1 \right), \qquad h_i = \sum_{j=1}^{i} d_j \tag{1.1}$$

In this model, there are N slabs apart from the semi-infinite substrate which is considered as slab[0]. ρ_i is the electron density from the i_{th} slab and σ_i is the interfacial roughness between slab $[i-1]$ and slab $[i]$. h_i is the location of the i_{th} interface (the electron density on the two sides are ρ_i and ρ_{i-1} respectively). The first interface is set

as 0, $h_1 = d_1 = 0$. d_i is the distance between the interface i and $i-1$. It can be easily verified that $\lim_{z\to-\infty}\rho(z) = \rho_0$ and $\lim_{z\to+\infty}\rho(z) = \rho_N$. This model is intuitive that each variable (ρ_i, d_i, σ_i) has its the physical counterpart (density, width, and roughness). It's also easy to convert the EDP to reflectivity curve with the master's formula due to the fact that the derivative of an error function is a Gaussian function. The *Master formula* for XRR is

$$R(q)/R_F(q) = \left| \int \frac{d\rho(z)}{dz} \exp(iqz) dz \right|^2 \tag{1.2}$$

Pluging in the EDP characterized by slab model,

$$R(q)/R_F(q) = \left| \sum_{i=1}^{N} (\rho_i - \rho_{i-1}) \exp(-q^2\sigma^2/2) \exp(iqh_i) \right|^2 \tag{1.3}$$

Several points are worthy to note. The master formula only works for $q >> q_{critical}$. By setting the roughness ($\sigma_i = 0$) to be zero and the all width ($d_i = 0$) to be a constant value that is below the spatial resolution of XRR, the slab model is converted to a new form that's widely used for model independent modeling and fitting. In some cases, a slab can be very thin while it's very rough on its two surfaces ($d_i < \sigma_i$ and/or $d_i << \sigma_{i-1}$). Though it's totally valid mathematically, the EDP will have a bump / dip which seems to be unphysical.

1.3. Calculating X-ray Reflectivity

Fitting XRR data requires many iterations of the reflectivity calculation. Thus, the calculation procedure must be fast and reliable. Parratt's recursive method can be implemented to easily achieve this goal. A N-layer film can be represented with scattering length density (SLD) as $\boldsymbol{\rho} = (\rho_0, \rho_1, \rho_2, \cdots, \rho_N)$, thicknesses of the layers as $\boldsymbol{d} = (d_1, d_2, \cdots, d_n)$, and roughnesses $\boldsymbol{\sigma} = (\sigma_1, \sigma_2, \cdots, \sigma_N)$. ρ_0 is the SLD for the substrate while ρ_N is SLD for the top layer which is usually air or solvent. σ_j is the roughness between the $(j-1)_{\text{th}}$ and j_{th} layer. The absorption terms are omitted in this thesis for simplicity because most of the data are taken in transmission cells where the attenuation from medium is almost a constant. The wave vector transfer for each layer is,

$$k_j = \sqrt{k_N^2 - 4\pi(\rho_i - \rho_N)} \tag{1.4}$$

and the reflectivity at the j_{th} interface is,

$$r_{j-1,j} = \frac{k_j - k_{j-1}}{k_j + k_{j-1}} \exp(-2k_j k_{j-1}\sigma_j^2) \tag{1.5}$$

$r_{-1,0}$, the reflectivity amplitude at the bottom of the substrate by this notation, is negligible, since it's far away from the film and its roughness is very high especially for unpolished substrates. The ratio of reflected and transmitted amplitude $X_{j-1,j} = R_{j-1,j}/T_{j-1,j}$ is then 0 for $j = 0$.

$$X_{j,j+1} = \frac{r_{j,j+1} + X_{j-1,j}\exp(2ik_j d_j)}{1 + r_{j,j+1}X_{j-1,j}\exp(2ik_j d_j)} \tag{1.6}$$

Recursively calculating the formula from $j = 0$ to $j = N$, the reflectivity is then

$$R = |X_{N-1,N}|^2 \tag{1.7}$$

1.4. Choice of Merit function

The merit function (or cost function) measures how much the fitted reflectivy curve deviates from the experiment data (or simply put, how good is the fit). It is key for XRR data analysis, mainly because $R(q)$ can decay over ten orders as a function of q. The standard choice is χ^2, defined as

$$\chi^2 = \frac{1}{N_d - N_p} \sum_{i=1}^{N_d} \frac{(R_{fit,i} - R_{exp,i})^2}{\sigma_{e,i}^2} \tag{1.8}$$

In which, N_d and N_p are the number of data points and the number of free parameters respectively, $R_{fit,i}$, $R_{exp,i}$, and $\sigma_{e,i}$ are calculated reflectivity, experimental reflectivity and uncertainty. Despite its well defined properties in statistics, χ^2 performs poorly, usually resulting in fitting the data only in the low-q region. This can be understood by the following argument: suppose the deviation at each point is proportional to $R_{exp,i}$ with a factor of α_i, and the uncertainty $\sigma_{e,i}$ is proportional to $\sqrt{R_{exp,i}}$ as one would expect for *Poisson distribution*, then $\chi^2 \propto \frac{1}{N_d - N_p} \sum_{i=1}^{N_d} \alpha_i^2 R_{exp,i}$. $R_{exp,i}$ decays as q_i^{-4}, making χ^2 ignore the residues at high-q region. Making things worse, real experiments don't only have statistical errors, but also systematic errors, originating from the nonuniformity of the X-ray beam and sample, mis-alignment of XRR setup *etc.* These factors are hard to take into the calculation of $\sigma_{e,i}$, but can contribute significantly to the deviation (the numerator term in Equation 1.8).

The logarithmic form merit function is a good candidate to overcome those problems,

$$\gamma^2 = \frac{1}{N_d}\sum_{i=1}^{N_d}\left[\log(R_{fit,i}) - \log(R_{exp,i})\right]^2 \tag{1.9}$$

The N_p term is not in the denominator to follow the conventions in MOTOfit [**6**]. Since most reflectivity curves are plotted in log scale, γ^2 is more intuitive to represent the deviation of fitting from the experiment data. Expanding γ^2 in Taylor series to the first order,

$$\gamma^2 = \frac{1}{N_d}\sum_{i=1}^{N_d}\left(\frac{R_{fit,i} - R_{exp,i}}{R_{exp,i}}\right)^2 = \frac{1}{N_d}\sum_{i=1}^{N_d}\alpha_i^2 \tag{1.10}$$

Thus, data points along the whole q-range contribute "evenly" to γ^2.

Another interesting property is that the logarithmic merit function is scale-free. Ideally the data from an XRR experiment should be normalized to the incoming photon number. The common monitor for incoming beam is the ion-chamber before the sample, which outputs a current proportional the flux of photons. To obtain the normalized reflectivity, a scaling factor is introduced, as well its uncertainty. Sometimes it's possible to use the reflectivity below the critical angle ($R \equiv 1.0$) to normalize (after foot-print correction), but for many cases the critical angle is too small (e.g. transmission cell with dense liquid). For applications that one needs to compare the fitting goodness (i.e. merit function) from one sample to another, this scaling procedure might lead to considerable error.

Assume the experiment reflectivity is offset by β_o, and the calculated reflectivity can be scaled by a variable β

(1.11)
$$\gamma^2 = \frac{1}{N_d}\sum_{i=1}^{N_d}\left[\log(\beta R_{fit,i}) - \log(\beta_o R_{exp,i})\right]^2 = \frac{1}{N_d}\sum_{i=1}^{N_d}\left[\log(R_{fit,i}) - \log(R_{exp,i}) + \log(\beta/\beta_o)\right]^2$$

β is also a fitting parameter which will converge to β_o, given that the model results in a good fit in the first place. Furthermore, the scale factor can be a function of q_i. For example,

(1.12)
$$\gamma^2 = \frac{1}{N_d}\sum_{i=1}^{N_d}\left[\log(R_{fit,i}/q_i^{-4}) - \log(R_{exp,i}/q_i^{-4})\right]^2$$

(1.13)
$$\gamma^2 = \frac{1}{N_d}\sum_{i=1}^{N_d}\left[\log(R_{fit,i}/R_{F,i}) - \log(R_{exp,i}/R_{F,i})\right]^2$$

In the equations above, Rq^4 and R/R_F are reflectivity divided by Fresnel reflectivity in the kinematic and dynamic approach respectively. These divisions are often used to remove the fast decaying baselines in reflectivity curves to manifest the features of interest. This mechanism is intrinsic for the logarithmic form γ^2 but not for the standard χ^2.

1.5. Statistical properties of logarithm Poisson distribution

The reflectivity R is related to the count of photons at the detector N by $R = N/N_0$. $N_0 = N_s \cdot N_i \cdot f(\theta)$, which are the scaling factor, ion chamber correction and footprint correction respectively.

(1.14)
$$P_N(N = n) = e^{-\lambda}\frac{\lambda^n}{n!} \qquad E[N] = \lambda \qquad Var[N] = \lambda$$

For the new variable $Y = \log(N)$, it's easy to verify that,

$$P_Y(Y = y) = e^{-\lambda} \frac{\lambda^{\exp(y)}}{[\exp(y)]!} \exp(y) = e^{-\lambda} \frac{\lambda^{\exp(y)}}{[\exp(y) - 1]!} \tag{1.15}$$

$$P_Y(Y = y) = e^{-\lambda} \frac{\lambda^{10^y}}{[10^y]!} 10^y \log 10 = e^{-\lambda} \frac{\lambda^{10^y}}{[10^y - 1]!} \log 10 \tag{1.16}$$

The denominator should be rounded to the nearest integer, to account for the machine precision and to calculate the factorial. To study this probability distribution, a numerical experiment with large sample size was conducted, as shown in Fig. 1.2. For the wide range studied, λ $sim[15, 5000]$, the histogram is always a bell shaped, and can be fitted nicely with a Gaussian function, $P_{\text{gaussian}}(y) = \frac{1}{\sqrt{2\pi}\sigma} \exp[-\frac{(y-\mu)^2}{2\sigma^2}]$. The fitting curves (dashed red) deviate from the analytical curves (solid blue, Eq 1.15) slightly at $\lambda \leq 100$ and become almost identical at $\lambda \geq 200$. To compare the deviation in detail, the expectation value and standard deviation value of the P.D.F. are calculated,

$$\mu_a = E[Y] = \sum y P_Y(y) \qquad \sigma_a = \sqrt{\sum y^2 P_Y(y) - E[Y]^2} \tag{1.17}$$

The summation range is limited to $\max\{0, \log(\gamma - 10\sqrt{\gamma})\}$ and $\log(\gamma + 10\sqrt{\gamma})$. The parameters from the Gaussian fits and the P.D.F. are plotted in Fig. 1.3. The μ values from both cases are almost identical, and follow the $\mu = \log(\lambda)$ curve closely. This is surprising because in Fig. 1.2, the maximal of P.D.F and fitting curves are not at the

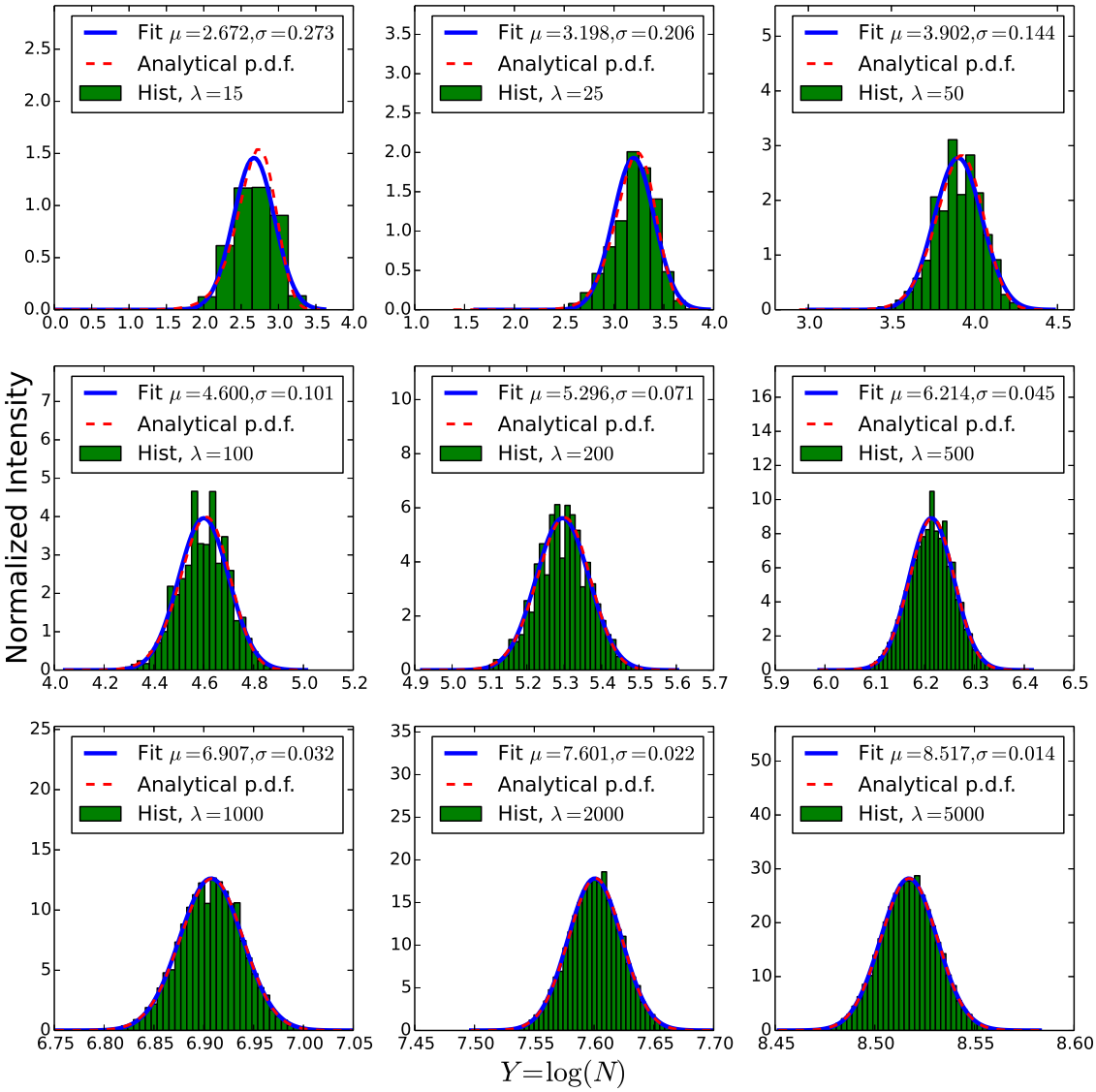

Figure 1.2. Numerical test with the Log *Poisson distribution*. For each plot, 1 million random samples are generated according to $N \sim Poisson(\lambda)$. The histograms show the distribution of $\log(N)$. Number of bins is $4\sqrt{\lambda}$, or 50 when λ is large. The blue lines are Gaussian fits, with fitting parameters (μ, σ) annotated in each figure. The red dashed lines are the analytical probability density functions in Eq.1.15.

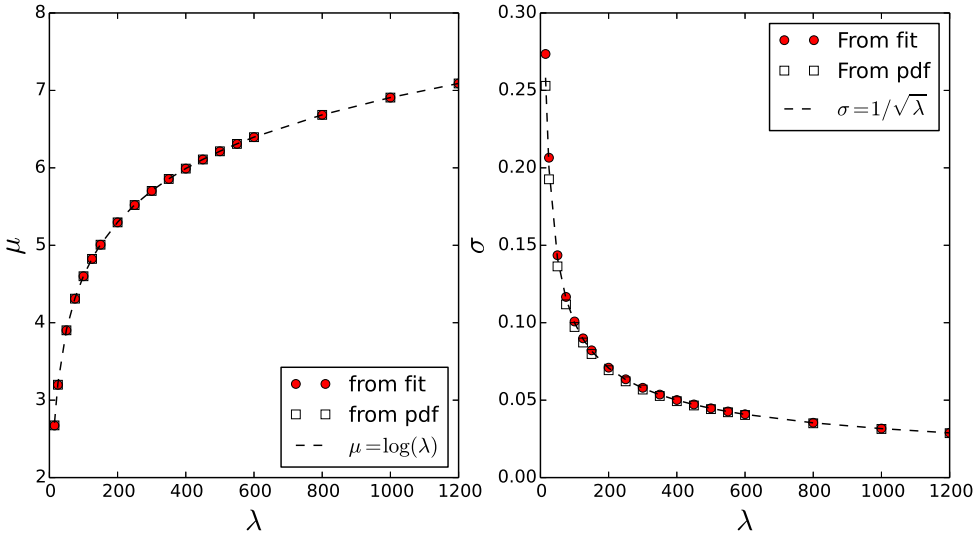

Figure 1.3. The mean and standard deviation of logarithm Poisson distribution as functions of λ. Red squares are values obtained from fitting with Gaussian function, shown in Figure 1.2. Empty squares are calculated directly from the probability density distribution (pdf) function. Dashed curves are the results from the first order approximation (described in the text).

same position at $\lambda \leq 100$. This is mostly likely due to the fact that the P.D.F is skew towards right side. σ from fitting is about 10% larger than from P.D.F. at λ. The difference quickly narrows and is negligible at $\lambda \sim 400$. The trend of σ can be characterized with $\sigma = 1/\sqrt{\lambda}$ when λ is large enough. Apply the following approximation[**7**],

$$\sigma = \sqrt{\mathrm{var}[\log(N)]} \approx \sqrt{(\log'(E[N]))^2 \mathrm{var}[N]} = |\log'(\lambda)\sqrt{\lambda}| = \frac{1}{\sqrt{\lambda}} \tag{1.18}$$

This approximation works well at large λ, where the "dispersion" of points ($\sqrt{\lambda}$) compared to the average value (λ)is small. The same analysis can be done with the $\log 10$ version of γ^2 1.16, which yields $\mu = \log 10(\lambda)$ and $\sigma = 1/(\lambda \log 10)$.

Let's revisit the definition of γ^2 in Eq 1.9. Though no uncertainty term explicitly appears in γ^2, it can be added simply by putting a global scaling factor, β_0, (and also put N_p, number of free parameters into γ^2)

$$\Gamma^2 = \beta\gamma^2 = \frac{1}{N_d - N_p} \sum_{i=1}^{N_d - N_p} \frac{[\log(R_{fit,i}) - \log(R_{exp,i})]^2}{1/\beta} \tag{1.19}$$

If β is chosen to be $1/\sigma^2 = \lambda$ ($\log_e$ version) or $1/\sigma^2 = \lambda \log 10$ ($\log_{10}$ version), the modified Γ^2 actually includes the measurement uncertainty. It should be noted that this equation is only for cases without background. In the next section, this λ has to be replaced by $\lambda_s + 2\lambda_n$ to account for the background.

This uncertainty is based on the assumption that all points have the same constant signal count. In a real experiment, the number of incident photons per exposure can be adjusted by applying X-ray filters and/or changing the time per exposure, to avoid saturating/burning the detector. In this thesis, the typical signal count using Pilatus 100K detector can vary from 10^5 at q_{critical} to a $10^1 \sim 10^2$ at $q_{\max}$. If the data points near critical angles and $q_{\max}$ are excluded, then the majority of points on XRR curves have counts of $10^3 10^4$. Interestingly, the empirical scale factors for most XRR fitting in this work is 10^3. This coincidence justifies the method of using scaled logarithm merit function.

1.6. Distinguishing the signal from noise in reflectivity measurement

In XRR experiments, photons are scattered not only by the surfaces of the samples, but also by other sources, including air, the edges of slits etc. As mentioned above, the

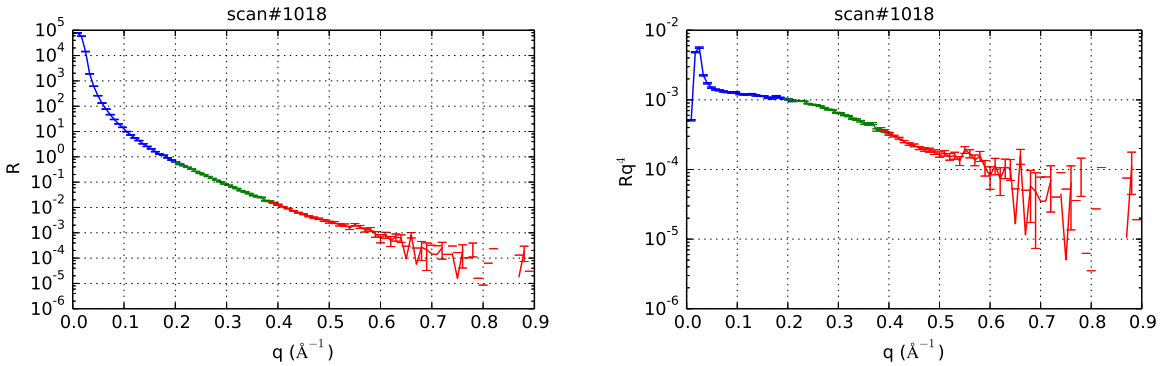

Figure 1.4. The extracted reflectivity of the XRR measurement of silicon oxide / TEHOS interface in a transmission cell (see text for detail) plotted as R and Rq^4. The data is corrected for footprint but not normalized.

specular reflectivity drops very fast, and at some point it's going to be comparable of the background before it gets smeared out. Fig. 1.4 and Fig. 1.5 show a typical example of signal vs noise as a function of q. Reflectivity was measured at the interface of silicon oxide and tetrakis-2-ethyl-hexoxysilane (TEHOS) liquid. The non-polar, sphere shape TEHOS molecules were found to form layering at the silicon surface by C.J. Yu in thin TEHOS film ($< 10^4$ Å)[**8**]. The layering spacing is about $10\mathring{A}$ (or $2\pi/10 = 0.628\mathring{A}^{-1}$ in XRR), about the size of TEHOS molecules. The isotropic scattering from 6mm TEHOS in the transmission cell is so much stronger than the signal of surface layering that, after background subtraction, the XRR curve is almost featureless in Fig. 1.4. In Fig. 1.5, the data recorded on the area detector are plotted with specular reflectivity and backgrounds marked with white boxes. At $q = 0.39\mathring{A}^{-1}$ and $q = 0.49\mathring{A}^{-1}$, the signal to noise ratio (S/N) is about 1.7857 and 0.3708. The center box is much brighter than the background boxes. At $q = 0.59\mathring{A}^{-1}$, S/N decreases to 0.0815, the signal is still distinguishable but a large error bar is expected. At $q = 0.59\mathring{A}^{-1}$, the middle box has about 80 more counts

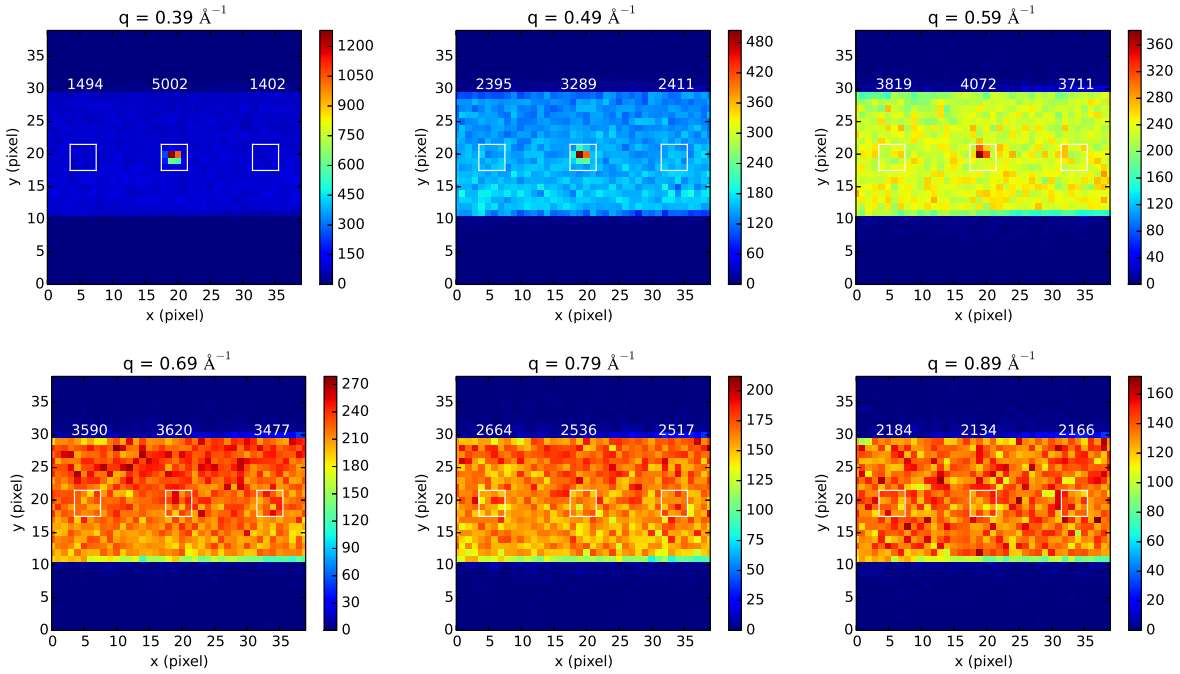

Figure 1.5. Specular reflectivity and background collected at different q_z on Pilatus 100K detector. The data is from a XRR measurement of silicon oxide (SiOH) and TEHOS liquid in a transmission cell. The center box is specular reflection and the two side boxes are for background. The count for each region of interest is annotated above. The x axis is χ direction and y axis is the $\theta - 2\theta$ direction. The stripes of blue are the anti-scattering slits located just before the detector.

than the average background, but it's impossible to tell which one is brighter by human eye. The standard deviation of background at $\lambda = 3533$ is about 59 and error bar is 73 (including error propagation). It's hard to say if the signal is real or just from the statistical fluctuation. At higher q one can even get negative signal counts by doing background subtraction, which isn't physically reasonable.

This example shows how the noise can overwhelm the reflectivity signal. It's necessary to quantify this process for applications like choosing the cut-off $q_{\max}$, classifying/disposing bad points and simulating artificial reflectivity data. Assuming the signal and background

are both Poisson distribution with μ equal to λ_s and λ_n, then the measured signal (s_m) can be expressed as,

$$s_m = s + n - n' \tag{1.20}$$

in which $s \sim \text{Poisson}(\lambda_s)$ and both n and n' are independent Poisson(λ_n). This kind of distribution was studied by Skellam[**9**]. The mean and standard deviation are λ_s and $\sqrt{\lambda_s + 2\lambda_n}$. The ratio of error bar and mean, $\alpha = \sqrt{\lambda_s + 2\lambda_n}/\lambda_s$. is plotted as a function of λ_s and λ_n in Fig. 1.6. For a fixed background, the ratio α raise quickly as λ_s drops to the standard deviation of background.

This analysis, however, is only valid in terms of statistics (i.e. with large sample size). For a real experiment, only one shot is taken. Thus, the fluctuation is much bigger even when α is low. An one-shot simulation is performed in Fig. 1.7 with α varied from 0.05 to 1.1. The 16×16 is the whole detector and the center 4×4 square is treated as the specular reflection spot. λ_n is set to be 1600 or 100 counts per pixel and λ_s is calculated by solving the α equation, $\lambda_s = (1 + \sqrt{1 + 8\alpha^2\lambda_n})/2\alpha^2$. Two sets of random Poisson distributed numbers are generated, superimposed and plotted together. By naked eye, it's difficult to identify the enhancement in the center box at $\alpha = 0.4$ and above. By increasing λ_n and λ_s proportionally to decrease α, which is equivalent to take longer exposure in experiments, it's possible to detect the difference. However, it takes quadratic time and radiation dose to half α which is sometimes infeasible for experiments.

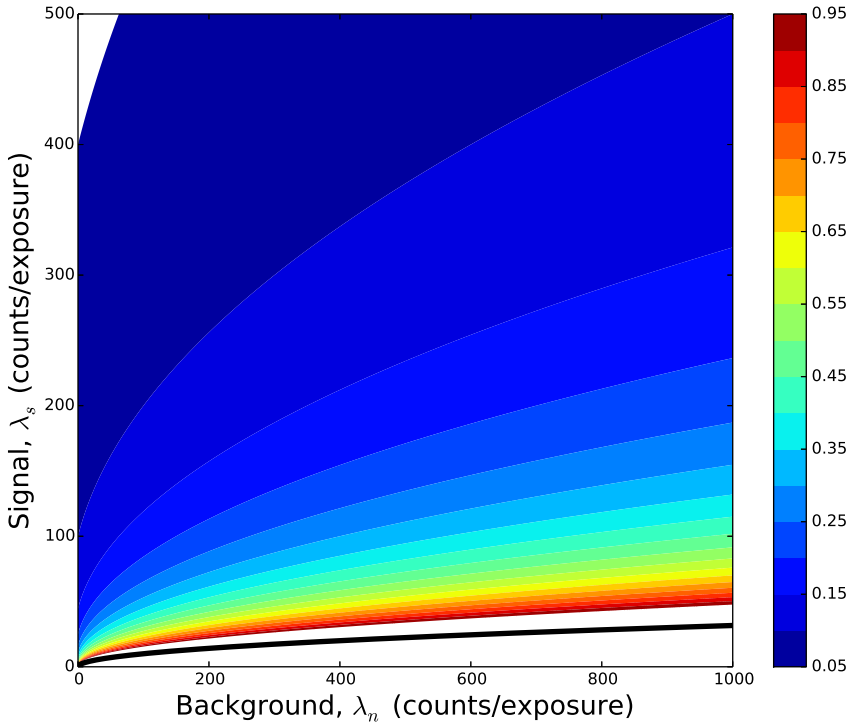

Figure 1.6. Contour of uncertainty to signal ratio, α. The black line is the uncertainty for background ($y = \sqrt{\lambda_n}$).

.

1.7. Generating Simulated XRR data

The key of generating simulated reflectivity data is to add the noise properly. Laub *et al* proposed a constant 2% error for all points[**10**]. van der Lee *et al* used a linearly increasing error, from 3 % at the $q_{\min}$ to 25% at $q_{\max}$[**11**]. As pointed out in the previous section, the signal and noise are both Poisson variables and their subtraction belongs to Skellam distribution. For a given a signal count λ_s and a background count λ_n, the measured signal λ_m is,

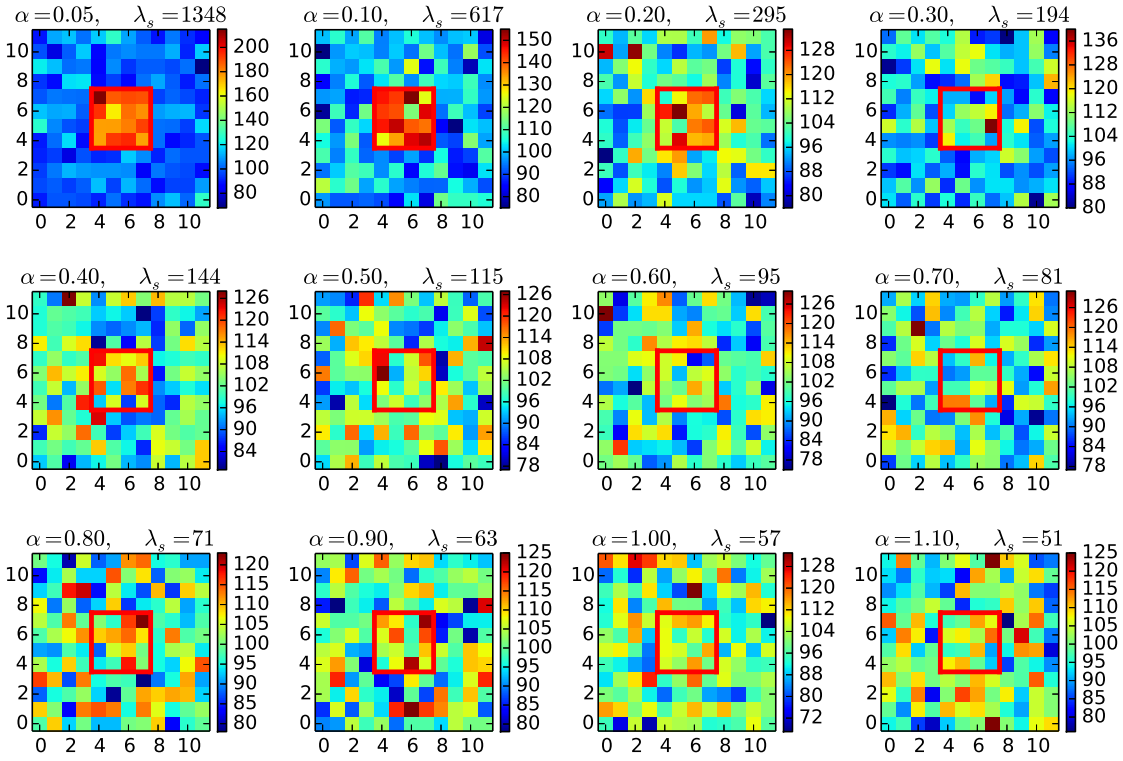

Figure 1.7. Simulation of reflectivity signal counts at different α. The background is fixed at 100 counts per pixel. The center box is the region of interest with 16 pixels, treated as the reflection spot.

$$\bar{\lambda_m} = \lambda_s \qquad \sigma(\lambda_m) = \sqrt{\lambda_s + 2\lambda_n} \tag{1.21}$$

Clearly the error is not a constant nor a linear function of q. To be more realistic, the simulated data is generated from the Skellam distribution with a constant background λ_n. A cutoff in $q_{\max}$ is set such that $\sigma(\lambda_m) = \alpha\lambda_m$. Assuming the background count is a constant, and $\lambda_s = R(q_{\max})N_0$, in which N_0 is the incoming flux. Solving the equation, $\alpha R(q_{\max})N_0 = \sqrt{R(q_{\max})N + 2\lambda_n}$,

$$N_0 = \frac{1 + \sqrt{1 + 8\alpha^2 \lambda_n}}{2\alpha^2 R(q_{\max})} \tag{1.22}$$

Now, for a given electron density profile, the exact reflectivity ($R(q_i)$) at q_i can be calculated with Parratt's optical method. The noise and signal count for this point will be, λ_n and $R(q_i)N_0$. By generating three Poisson variables (n_0, n_1, s_0) with $\lambda = (\lambda_n, \lambda_n, R(q_i)N_0)$, the simulated reflectivity and its uncertainty will be,

$$R_s(q_i) = \frac{n_0 + s_0 - n_1}{N_0} \qquad \Delta R_s(q_i) = \frac{\sqrt{n_0 + n_1 + s_0}}{N_0} \tag{1.23}$$

This procedure generates artificial reflectivity data with the theoretical statistical properties of an ideal XRR experiment. It's even better than real experiment data since it lacks systematic errors such as those originate from X-ray beam's uniformity and stability. The artificial reflectivity data is useful in several ways. For given surface structures, either from molecular simulations or theoretical predictions, one can use the artificial reflectivity data to determine the XRR pattern(if any). It can also be used to evaluate the efficiency of a fitting program, which will be the theme for the next chapter.

CHAPTER 2

Resolution of XRR technique

2.1. Introduction

Despite the straightforward experimental setup, XRR isn't so intuitive when it comes to the interpretation of the reflectivity data. Firstly, the maximal momentum transfer for XRR ($q_{\max}$) is limited by the interfacial roughness as well as the flux of the X-ray source. For single crystal substrates, such as rutile and mica, it can reach as high as 8 Å^{-1}. But more commonly, for samples prepared on a prime grade silicon wafer, it's usually reduced to 1 Å^{-1} or less. Additionally, the X-ray detectors can only record the number of photons without their phase information, which means the reconstructions of real space electron density profiles from the XRR data are inverse problems. In other words, many different models will yield the same XRR data within certain error, but they are not necessarily corresponding to the physical structures.

For an optical telescope, the resolution is limited by the diffraction limit, $\Delta\theta = 1.22\lambda/nD$. λ, n, D are the wavelength of light, the refraction index and the diameter of the lens. A light source with shorter wavelength (larger wave number) would yield better resolution. Similarly, XRR measurement also has limited wave transfer ($q_z \leq q_{\max}$) due to the fast decaying reflectivity signal. The theoretical resolution limit, $\Delta = \pi/q_{\max}$, derived directly from Fourier analysis, is a widely used measure of the spatial limit XRR

can detect. As mentioned in the previous chapter, the last few points in XRR data including the $q_{\max}$ point suffer considerable fluctuations. This makes $q_{\max}$ not so robust. In addition, to fit a complex film (e.g. a multiple-layer film) requires multiple variables which may have strong correlations with each other. Another obvious flaw with $\Delta = \pi/q_{\max}$ is that it doesn't have any terms involving the contrast of the electron densities. If a thin film has several substructures, the XRR pattern is largely determined by the interfaces with higher density contrast, under the perturbations from the low contrast interfaces.

In this chapter, numerical experiments are conducted to explore how well does a fitting procedure retrieve the real electron density profile. The simplest slab model with just one slab is used to generate artificial XRR data with proper statistical fluctuation, using the method described in the previous chapter. The profiles obtained by fitting are compared to the profiles that generate the XRR data to determine the fitting errors.

2.2. Effect of slab width

The single slab model assumes an interfacial layer with uniform electron density between the substrate and the top media (air or solvent). It is very useful to analyze the XRR data of films without stratification or gradient in electron density. This model can be widely found in self-assembled monolayers[**12**], deposited films[**13**], surface oxidation[**14**] *etc.* It's also a great starting point to analyze more complex films.

A single slab model has four parameters, $(\rho_x, D, \sigma_1, \sigma_2)$, which are the electron density and thickness of the film, roughnesses of the interface between substrate/film, and film/top media respectively. The densities of top media (ρ_s) and substrate (ρ_t), which

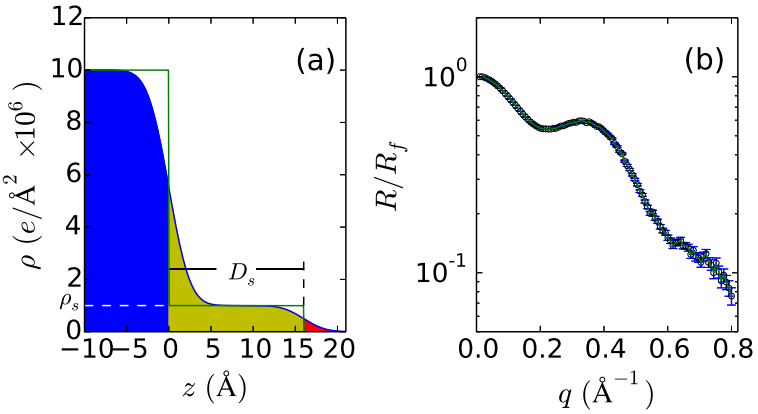

Figure 2.1. An example of simulating reflectivity data. Electron density profile with known parameters is plotted in the left panel, with blue slab as the substrate, yellow slab as the slab to be fitted and red slab as the top medium. The green curve outlines the density profile if there are no roughness between slabs. The substrate is set to be the density of water (which is a typical number for soft matter) while the top medium is air. This density profile is used to simulate the reflectivity data shown in the right panel. The simulating process is described in the text.

can be calculated easily according to the material composition, are taken as fixed fitting parameters. The electron density contrast is defined as $\gamma_{ct} = (\rho_x - \rho_t)/(\rho_s - \rho_t)$, which is fixed $\gamma_{ct} = 0.1$. $q_{\max}$ is set at 0.8Å^{-1}, corresponding to resolution of $\pi/q_{\max} = 4\text{Å}$. The interface roughnesses are set at $\sigma_1 = 2.0\text{Å}$ and $\sigma_2 = 3.0\text{Å}$, which are typical values in XRR experiments.

A series of simulated reflectivity data with widths (D_s) ranging from 1Å to 16Å are generated and fitted with one-slab model. Figure 2.1(a) shows an example of postulated density profile and the resulting artificial X-ray reflectivity. The assumed density profile consists of a semi-infinite substrate of density 10^{-5} electrons/Å^2, covered by a 16Å thick thin film with density 10^{-6} electrons/Å^2. The resulting reflectivity data are shown in Figure 2.1(b) with error bars. The data are generated up to a finite maximal wavevector

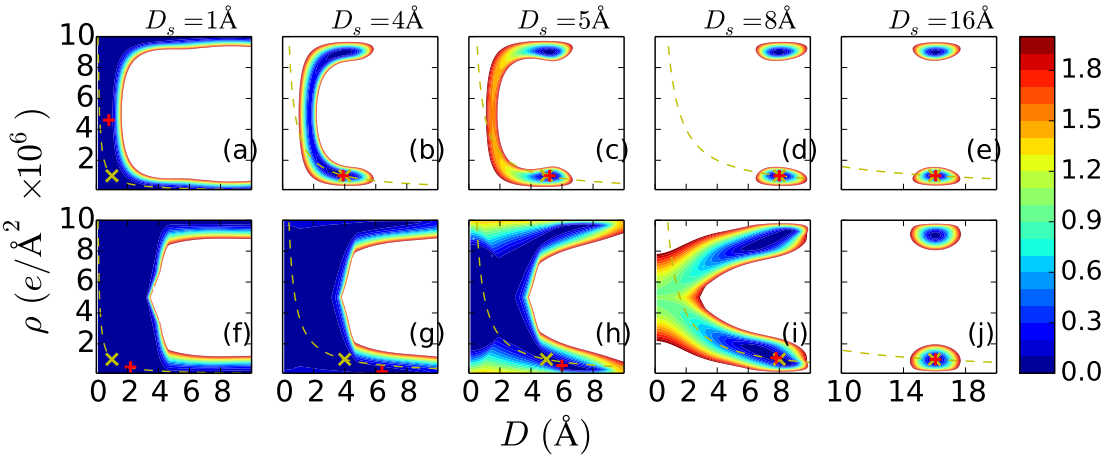

Figure 2.2. Contours of merit function on $D - \rho$ plane. The simulated profiles are generated with constant contrast and varied width D_s, which is labeled on the top. (a)-(e) are fittings with fixed roughness values while in (f)-(j), the roughness, σ_1 and σ_2, are allowed to vary freely during fitting. The red christcross indicates the best fitting parameter. The yellow X shape marks the exact parameters used to generate the simulated data. The yellow lines follow the equation $D \cdot \rho = D_s \cdot \rho_s$.

transfer ($q_{\max}$), since reflectivity intensities drop rapidly and the range of data is always limited. Other simulated data (not shown) were generated using the same qualitative model but varying the parameters, as discussed further below.

Instead of just reporting the parameters that yield the global minima (best fit), we report the fitting results as contours of merit function value in $D - \rho$ plane, as shown in Figure 2.2. The other two parameters (σ_1, σ_2) are fixed in the upper panels but are allow to float in the lower panels in Figure 2.2. In the upper panels, the only two parameters that are free to vary during fitting are D and ρ . At $D_s = 1$Å, the parameters that yields good fits (the blue region) correspond to profiles that either have negligible D or have negligible electron density differences.

The parameter for the best fit marked by the red crisscross is not located near the yellow cross which represents the profile that generates the XRR data in the first place. In other words, it's not possible to distinguish the layer. When D_s increases to 4Å, just about the theoretical resolution, the contour changes to "C" shape. The values of merit function at both ends of the C shape are slightly lower than those in the middle. The global minimal is next to the right position, suggesting the fit is able to find the real profile but with considerable error (the blue region stretches across the plot). Just by increasing D_s by 1Å, the color separates, manifests two islands of good fitting region. When $D_s = 8$Å, twice the theoretical resolution, the connecting part of the islands disappears. The shape of the islands is almost elliptical with orthogonal axes in the $D - \rho$ plane, suggesting weak correlation between D and ρ.

However, in practice, how rough the interfaces are often unknown. Thus, each interfacial roughness should be treated as an independent variable within reasonable range. The lower panels (f) (j) of Figure 2.2 shows the contour of fit with σ_1 and σ_2 as hidden float variables. To be more specific, at each point on the contour, σ_1 and σ_2 are allow to vary until the best local minima is reached. The contours at D_s =1Å and 4Å are almost identical. Both of them have a wide blue area below $D_s = 4$Å and two arms extending along the density line that corresponding to zero contrast. The low γ^2 region shrinks at 5Å, but it's not until D_s =8Å(twice the theoretical resolution) that the global minima start to yield the real profile.

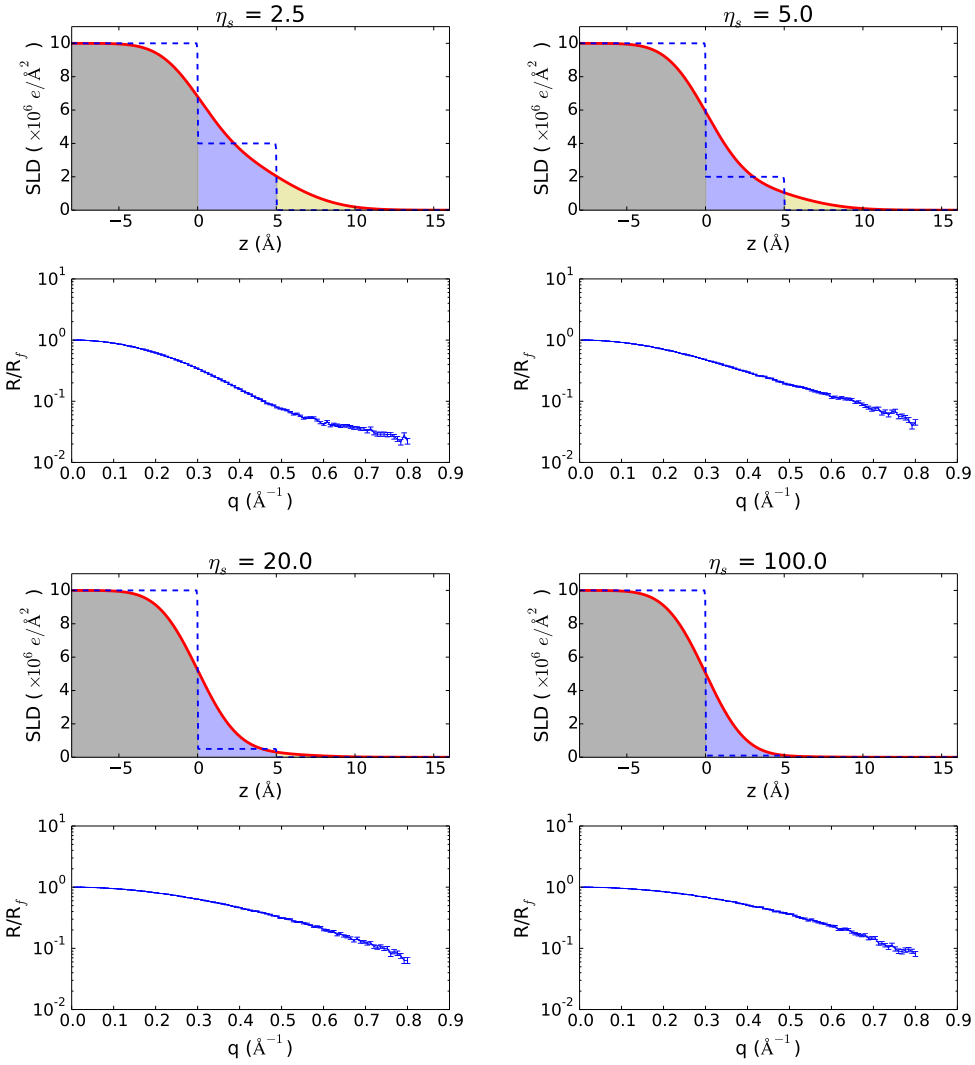

Figure 2.3. SLD profiles with different contrast (η_s). The black and blue are the substrate and the film being studied. Due to the nonzero interfacial roughness, the profiles extend to the top medium (air). The blue dashed lines are profiles if all interfaces are infinitely sharp. The simulated reflectivity curves are calculated following the procedure described previously.

2.3. Effect of contrast

Reflectivity patterns originate from the interference of X-rays(neutrons) at the interfaces where the scattering length density (SLD) on its two sides are different. Generally, higher contrast results in higher interference amplitude which often yields stronger reflectivity pattern. Unlike the neutron reflectivity where one can adjust the SLD (even flip its sign) of the film under study by deuterating, X-ray is only sensitive to the electron density (assuming the photon energy is far away from the absorption edge) which is determined by the elements in the material. Nevertheless, one can still change the contrast by choosing a different substrate or top medium. For example, the thin film under study can be either deposited onto a metallic substrate with very high electron density, or deposited onto to a sapphire/quartz/silicon with much lower electron density. Thus, a better understanding of how the SLD contrast affects the reflectivity is not only important to the data analysis but also poses some general guidance of which substrate to choose at the design stage of the experiment.

A series of SLD profiles with different contrasts are generated while keeping the rest variables fixed. The fixed variables include the SLD of the substrate (half of silicon SLD) and top medium (vacuum, zero), the roughness of the interfaces (2Åand 3Å), the film thickness (5Å) and the maximal q range ($q_{max} = 0.8\text{Å}^{-1}$). The control of the contrast, defined as $\eta_s = \rho_f/\rho_s ub$, is made possible by varying the film SLD (ρ_f).

The SLD profiles as well as the reflectivity curves simulated from those profiles are plotted in Figure 2.3. At $\eta_s = 2.5$, the highest contrast in this study, the reflectivity curve shows a dip around $\pi/5 = 0.63\text{Å}^{-1}$. This is from the strong interference of the two interfaces separated by 5Å. However, as η_s increases to 5.0, this dip is almost invisible.

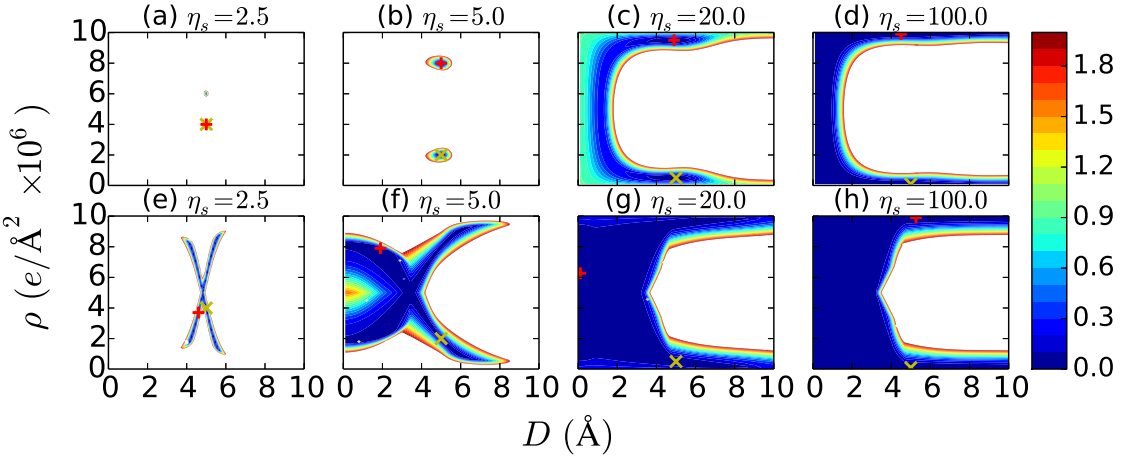

Figure 2.4. Effect of density contrast ($\gamma_{\rm ct}$) on the landscape of merit function. Two schemes were used to fit the reflectivity data. For (a)-(d), the roughness are fixed while for (e)-(h), the roughnesses are treated as variables. See the text for details. The yellow **X** and red + are the exact parameter of the SLD profile and three global minima.

At even higher η_s, the reflectivity curves are almost featureless. The ratio of reflectivity amplitude of the two interfaces at contrast η_s are $1 : (\eta_s - 1)$. A ratio closer to $1 : 1$ will have the stronger interference between interfaces and result in stronger reflectivity patterns.

By applying the contour-searching technique described in the previous section, the simulated reflectivity data are fitted with one-slab model with four parameters $(\rho, D, \sigma_1, \sigma_2)$. As shown previously, whether the interfacial roughnesses are fixed or not changes the contour landscape significantly. The results are summarized in Figure 2.4. At $\eta_s = 2.5$ and 5.0, the fixed fitting would result in two distinct point shaped minima, indicating the values of ρ and D can be determined with high accuracy by fitting. However, if the roughnesses are considered as variables, which they should be for real data analysis, the

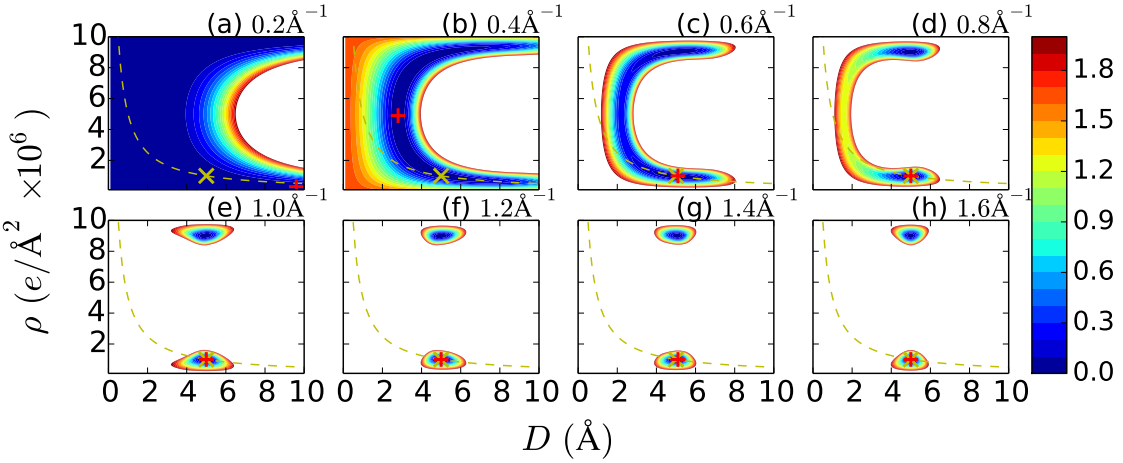

Figure 2.5. Contours for merit function for simulated data with $q_{\max}$ ranging from 0.2 to 1.6 $\AA^{-1}$. The density contrast γ_{ct} is set at 0.1 and the simulated slab is set to be 5Å. The roughness of the two interfaces are both 2Å.

good-fit regions (blue part on the contour) transform into X-shape. The combinations of (ρ, D) along the X-shape, with the help of hidden variables σ_1 and σ_2, can produce reflectivity curves that resemble that simulated data. A normal fitting program which only seeks the global minima doesn't necessary yield the real profile. This is again verified in Figure 2.4, the red + which represents the global minima doesn't follow the yellow cross which is the real profile.

When η_s increases to 10 and 100, the contrasts between interfaces are reduced significantly. The simulated reflectivity data are basically featureless, as shown in Figure 2.3. Fitting of the reflectivity data can't retrieve the real profiles, even if the roughnesses are fixed.

2.4. Effect of q range

Reflectivity curves from non-smooth interfaces usually decay faster than the Fresnel reflectivity, which falls as $R_F(q) \sim 1/q^4$, in which q is the wave vector transfer. This nature makes the measurements of reflectivity data reaching high-q extremely demanding. Even with the state-of-the-art synchrotron sources, one can't increase $q_{\max}$ to any degree, not to mention the neutron sources with a much lower flux. The most feasible way to obtain data with wider q-range is to do experiment on smooth substrates.

Silicon wafers and sapphire are two most common substrates that can achieve atomic flatness (root mean square roughness). The prime grade silicon wafers after Piranha cleaning can reach 2Å, while sapphire can reach 1Å. When a thin film is deposited/self-assembled onto the substrates, one or more rough (compared to the substrates) interfaces are introduced, which often significantly reduces the q-range.

In this section, the effects of q-range on the reflectivity data analysis is investigated by fitting the artificial data. A single slab model with width of 5Å, electron density of 10 percent of the substrate, and interfacial roughness of 2Å, is used to generated simulate XRR data with $q_{\max}$ ranging from 0.2Å^{-1} to 1.6Å^{-1}. As mentioned in the previous section, there are four variables for a single slab fitting, $(\rho, D, \sigma_1, \sigma_2)$. All four variables are allowed to vary in this section. Not surprisingly, the contours of merit function show (Figure 2.5) a clear dependence on $q_{\max}$.

When $q_{\max}$ is far below the resolution limit of $q_{theory} = \pi/5.0 = 0.6\text{Å}^{-1}$, it's virtually impossible to identify the real profile. As $q_{\max}$ increases to q_{theory}, the region of good fits shrinks significantly. Beyond $q_{\max}$, the contour transforms into two separate islands which are equivalent in producing the simulated data.

2.5. Patterson function for X-ray reflectivity

Patterson function, the Fourier transform of scattering intensity, is a convenient way to solve the crystal structures [**15**]. When it comes to XRR, which is a special case of crystallography that only measures the out of plane diffraction, Patterson can also be applied.

$$
\begin{aligned}
(2.1) \quad P(s) &= \int \frac{R(q)}{R_F(q)} \exp(iqs) dq = A \int \left| \int \frac{d\rho}{dz} \exp(iqz) dz \right|^2 \exp(iqs) dq \\
&= A \int \left[\int \frac{d\rho(z)}{dz} \exp(iqz) dz \right] \left[\int \frac{d\rho(z')}{dz'} \exp(-iqz') dz' \right] \exp(iqs) dq \\
&= A \int \int \frac{d\rho(z)}{dz} \frac{d\rho(z')}{dz'} \delta(z + s - z') dz' dz \\
&= A \int \frac{d\rho(z)}{dz} \frac{d\rho(z+s)}{dz} dz
\end{aligned}
$$

A is a proportionality constant. The integration goes from minus infinity to infinity in the momentum transfer while the real data only has limited q-range. In practice, the reflectivity beyond $q_{\max}$ is extrapolated until it's far beyond the characteristic length of the system under study. In addition, it is mirrored so that its Fourier transfer is a real function of s.

In the cases which have pronounced XRR pattern (or equivalently the film is thick), the Patterson function can be used to estimate the interfacial structure [**8, 16**] or even to retrieve the EDP directly [**17**]. However, for XRR data with weak patterns or limited q-range, conclusions drawn from the Patterson function are questionable. In this section,

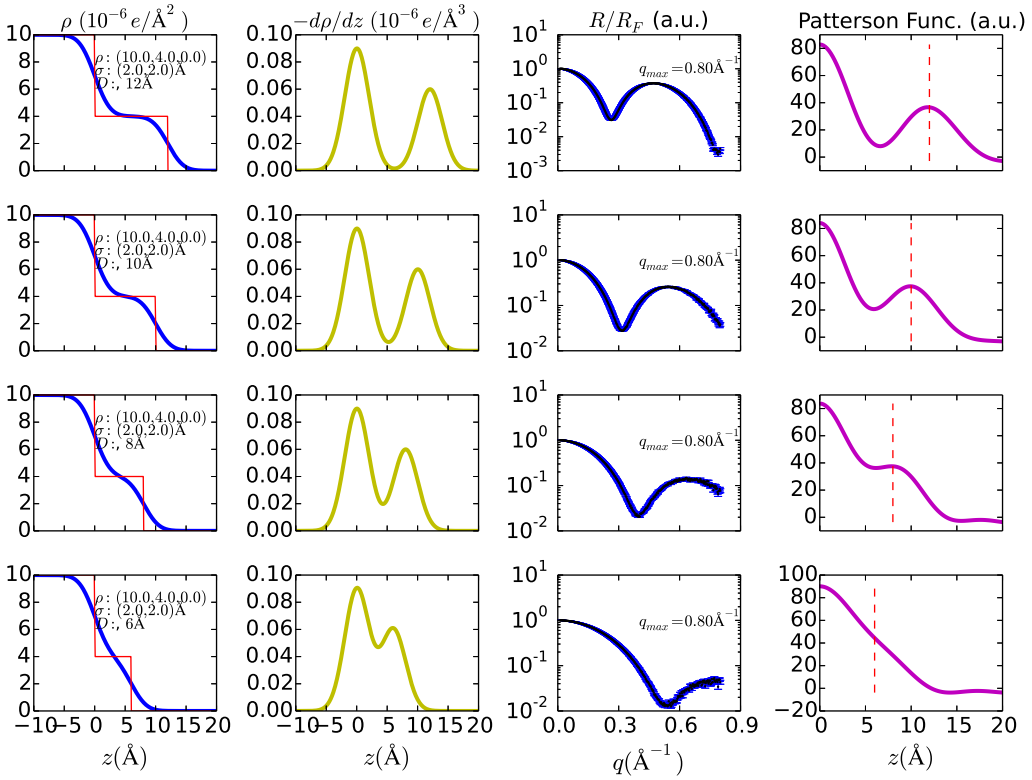

Figure 2.6. Effect of slab width on the Patterson function. The first two columns are the EDP (blue lines) and differential EDP (yellow lines). The profiles are listed in the first column figures. The red lines are EDP by setting the roughness for each profile to be zero. The third column is reflectivity curve normalized to Fresnel reflectivity. The procedure of producing reflectivity with fluctuation is described in the text. The last column is the Patterson function calculated from the simulated data, with red lines indicating the slab width.

those edge cases are studied with numerical experiments on a single slab model with two interfaces to find out under what conditions the Patterson method fails.

The four parameters used to define the XRR data are slab width(D), slab density(ρ), roughness(σ_1, σ_2) and the maximal q-range ($q_{\max}$). σ_1 and σ_2 are set to be equal to each

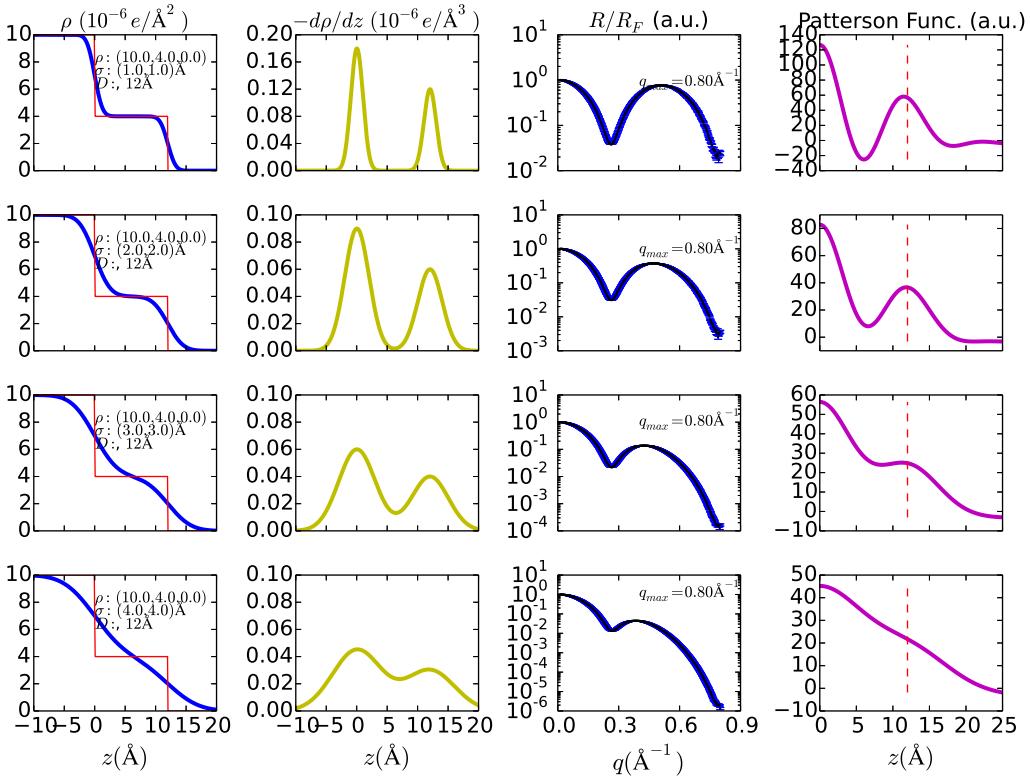

Figure 2.7. Effect of interfacial roughness on the Patterson function. The curves in each panel are explained in Figure 2.6.

other and are studied together. The effect of each parameter to the Patterson is studied while keep the rest three fixed.

As shown in Figure 2.6, the Patterson function is able to indicate the right slab width when it's at least 8 Å. When the slab width is 6 Å, due to the smearing effect due to the interfacial roughness, the EDP profile looks like that of a single interface. Nevertheless, the differential EDP still has two distinct peaks which start overlapping with each other, and the XRR data shows a clear dip due to the 6 Åslab. However, the Patterson function calculated from the XRR data fails to pinpoint the slab width.

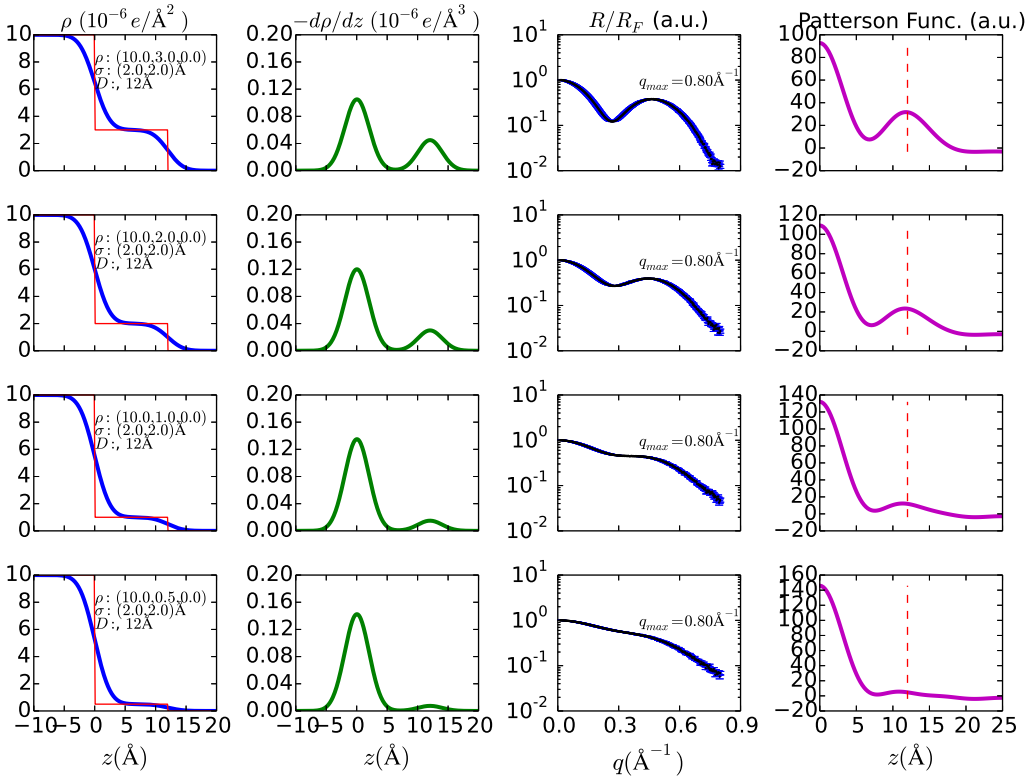

Figure 2.8. Effect of contrast in electron density on the Patterson function. The curves in each panel are explained in Figure 2.6.

Alternatively, when the roughness increases while the slab width is fixed, the Patterson function behaves in a similar way, shown in Figure 2.7. It can be concluded that the overlap of the two peaks in the differential EDP leads to the failure of Patterson function.

Furthermore, the electron density differences for the two interfaces which define the interference amplitudes are varied in the rows of plot in Figure 2.8. As the contrast decreases, the peak in the Patterson function weakens but stays at the correct position until it becomes indistinguishable. Thus, it can be inferred that the weak (in terms of

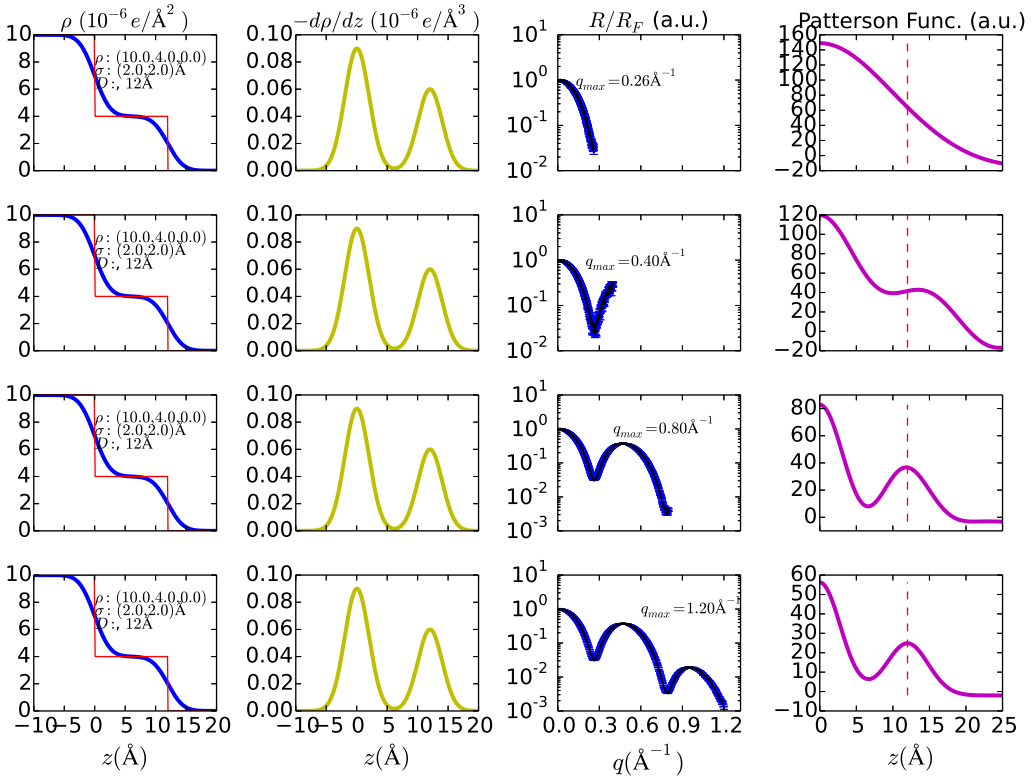

Figure 2.9. Effect of $q_{\max}$ of XRR data on the Patterson function. The curves in each panel are explained in Figure 2.6.

electron density contrast) structures in complex films (with multiple slabs) cannot be determined reliably with the Patterson function.

Finally, XRR data with a very limited q-ranges limit the usage of the Patterson function. In Figure 2.9, at $q_{\max} = 0.26$ Å^{-1}, the theoretical resolution limit to discern the 12Å structure, XRR data just reaches the first minimum while Patterson function is featureless. As $q_{\max}$ increases to 0.4Å^{-1}, Patterson function has a peak which isn't at the correct position. It's not until $q_{\max}$ reaches 0.8Å^{-1} that the Patterson function starts to report the right slab width. This demonstrates that the Patterson function works only with XRR data with complete reflectivity patterns.

2.6. Conclusion

Using the numerical experiment methods, we demonstrate how susceptible the interpretation of ill-defined XRR data can be. For XRR studies of soft matter, it often happens that the structure of interest is very small in dimension or very weak in contrast. To analyze such data, one must pay extra attention to reach robust conclusions and avoid problems such as over-fitting.

CHAPTER 3

Solvent Distribution Near Hydrophobic Surface: An X-ray Reflectivity Study

3.1. Introduction

Interactions of solvent-hydrophobic surfaces are key to protein functions [**18**], drug delivery[**19**], coating, self-assembly[**20**] and omnipresent applications in chemical engineering. A simple but important question, how the solvent molecules next to the hydrophobic surface are distributed, is still under debate. X-ray reflectivity (XRR) has been proven a successful technique to resolve the interface *in situ*. However, since the interfacial region is only a few angstroms thick and has low density contrast from the bulk, XRR can't reliably determine either thickness or density change, but instead the effective thickness, defined as, $D_e q = D_g(\rho_s - \rho_g)/\rho_s$. D_g, ρ_s are the thickness and electron density for the depletion region, while ρ_s is the electron density for the bulk solvent.

Water, the most important and ubiquitous solvent, has been found to have a density depletion region ("*gap*") when it touches a hydrophobic surface[**21, 22, 23**]. Ethanol[**24**] on octadecyltriethxysilane (OTE) SAM was also found to have an effective depletion width of 1.3-1.8 aÅ. Another alcohol, octadecanol[**25**], melted on octadecanol-SAM on silicon, was found to have a gap of 1.7 Å at 63 degree and shrinked to 0.6 Å at 100 degree Celsius. However, Ocko et al[**26**] pointed out that the gap found in various systems originating from hydrogen terminated SAM's and solvent's molecules at the interface,

creating a region contains very few electrons. They estimated the gap parameter would be 2.27 Å wide and 50% of the bulk density, corresponding to 1.0 Å effective width. This estimation, however, is based on the assumption that the SAM is perfectly smooth. The surface roughness of SAM is around 2-3 Å, comparable to the length scale of gap caused by hydrogen bonds. The solvent molecules, if they have chemical affinities to the SAM, prefer to locate near the SAM and smears out the electron density contrast. This is especially true for solvents with small volumes and at low temperature when the thermal fluctuation is small.

In this chapter, XRR experiments are performed to study the interface between n-octadecyltrichlorosilane (OTS) self-assemble monolayer (SAM) and several very common solvents, including both polar and nonpolar ones. Instead of reporting the single "*best fit*", the contours of fitting merit function are plotted, providing a clear discription of the gap region.

3.2. Experimental details

The OTS films were prepared following Wang et al with a few adaptions[**27**]. We used high-quality thermal silicon oxide instead of silicon with native amorphous oxide. This is to avoid the extra silicon/silicon oxide interface which sometimes yields unphysical roughness in XRR data analysis[**23**] and the extra electron density depletion between the silicon and silicon oxide interface[**23, 28**]. This is crucial for reflectivity data analysis, since this extra region would introduce 3 more parameters, which may smear the subtle

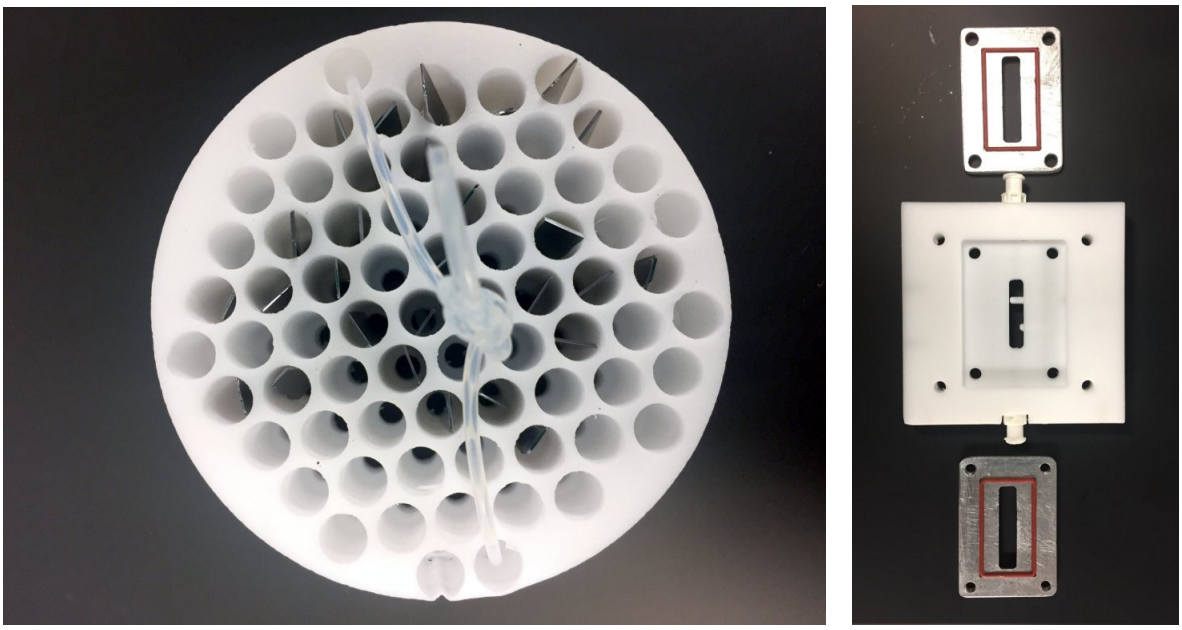

Figure 3.1. Left: the Teflon chamber for substrate cleanning and OTS coating. Right: the transmission cell and two aluminum covers used in this study.

change caused by the gap. It also makes the comparison of reflectivity data from one sample to another possible since one doesn't need to worry about changes in the substrates.

The thermal silicon oxide wafers were cut to $5mm \times 18mm$ chips and placed into a Teflon-made sample chambers with honeycomb cells. The chips were cleaned twice with Piranha solution (7:3 sulfuric acid: hydrogen peroxide) for 30 mins. This process violently removes all organic residues on the surface. After cleaning, the chips were rinsed with pure water 10 times, before being stored in pure water.

The OTS sample quality is very sensitive to the water content in the chemical and substrates, as pointed out by Wang et al. The chips were dried using dry nitrogen flow. Chips,

Teflon sample holder and the glass jar were placed into an oven at 150 degrees for 15 minutes. They were cooled down to room temperature using dry nitrogen. The anhydrous solvents for OTS solution, heptane, chloroform and carbon tetrachloride were purchased from Sigma Aldrich and used without further purification. 0.25mL n-octadecyltrichlorosilane (OTS, Gelest, 97 %) was mixed with 100mL heptane, 15mL chloroform and 10mL carbon tetrachloride to make 0.5mM OTS solution. The chips were submerged in the OTS solution in a glass jar which was sealed with a Teflon cap and placed into a desiccator. After 48 hours, the sample holder together with the chips was pulled out of OTS solution and immediately rinsed with anhydrous heptane 3 times. The samples were dried again with nitrogen and stored in a desiccator.

The 5mm chip coated with OTS was mounted by a screw to the transmission cell, made of Teflon. The cell was sealed by clamping two aluminum covers (with ultra-compressible O-rings) against Kapton windows (which was cleaned with methanol and acetone sonicating). About 2mL solvent (water, acetone, methanol, ethanol, 1-propanol, pentane, hexane, heptane) was injected into the transmission cell with a clean glass syringe. The solvent covered the OTS sample, leaving no air bubble in the transmission cell. X-ray reflectivity measurements were performed at 12BM-B, Advance Photon Source, Argonne National lab, at energy of 19.5 KeV. The beam was focused to be 0.5mm by 0.5mm. A Pilatus 100K detector was used to collect specular reflectivity and background simultaneously.

The electron density of the OTS SAM/solvent(air) system is modelled by a slab model described elsewhere. The reflectivity curve of the slab model is calculated by the Parratt's recursive method. The logarithmic merit function, γ^2, was employed to capture the

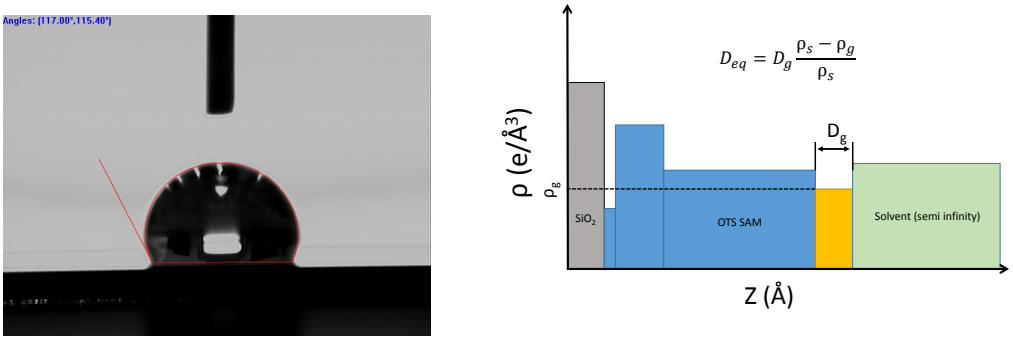

Figure 3.2. Left: contact angle measurement on a OTS sample. The 117-degree contact angle indicates the high quality of the samples. Right: the electron density profile used to characterize the OTS film in contact with a solvent. The interfaces are without roughness smearing for clarity. The gap layer with width of D_g and electron density of ρ_g is introduced to better fit the experimental data.

goodness of fitting over wide q-range. Analysis in Chapter 1 shows the logarithm of a Poisson distribution is approximately proportional to the standard χ^2. The scaling factor found in many fittings is about 1000, roughly the counts on the detector. Thus, similarly to the standard χ^2, we can define the error bar of a fitting variable by finding the points that increase γ^2 by 1.00, 2.71 and 6.63, corresponding to 68.3%, 90.0% and 99.0% of probability[**29**]. Figure [**?**] shows how the fitting is qualitatively affected by the augmentation.

3.3. Result and Discussion

3.3.1. Dry OTS film

The quality of OTS film is key for the liquid-solid interface studies. This is especially true for reflectivity studies since it averages a arge footprint on the sample. As shown

by Poynor et al[**22**], samples with bad quality show totally different reflectivity patterns. Our samples were examined with contact angle measurement, resulting with 115+ degree angle, in agreement with the literature [**26, 27, 30**]. The reflectivity measurements were also performed on OTS films without any solvent (dry OTS), showing clear oscillation up to 0.84 1/A. Following Steinrück et al[**31, 28**], the dry OTS XRR was fitted with a 3-slab model. The first slab with low density that represents the silane anchoring to the substrate. The second slab accounts for the Si-O-Si crossing, and the third slab for the OTS hydrocarbon chain. The fitting parameters of dry OTS are in good agreement with other published result. The contact angle measurement and XRR on dry film prove that our samples are very hydrophobic and uniform both locally and over the whole sample.

3.3.2. OTS film in solvents

For the XRR data with solvents, an additional layer (gap layer) with electron density (ρ_g) and width (D_g) is introduced in fitting to account for the possible density depletion region at the interface. As mentioned previously, this gap feature is weak both in the density contrast as well as length scale. The best-fit isn't able to characterize the feature and the strong correlation between fitting variables. Instead, we do fitting on each point in the $D_g - \rho_g$ plane and plot the contour of the merit function.

The fitting parameters from the dry sample are the starting points to analyze the data with solvents. However, one shouldn't fix every parameter for the OTS film for two reasons. Firstly, despite the high quality, it's still possible that some parameters, for example the roughness of the substrate, would vary from sample to sample, even if the

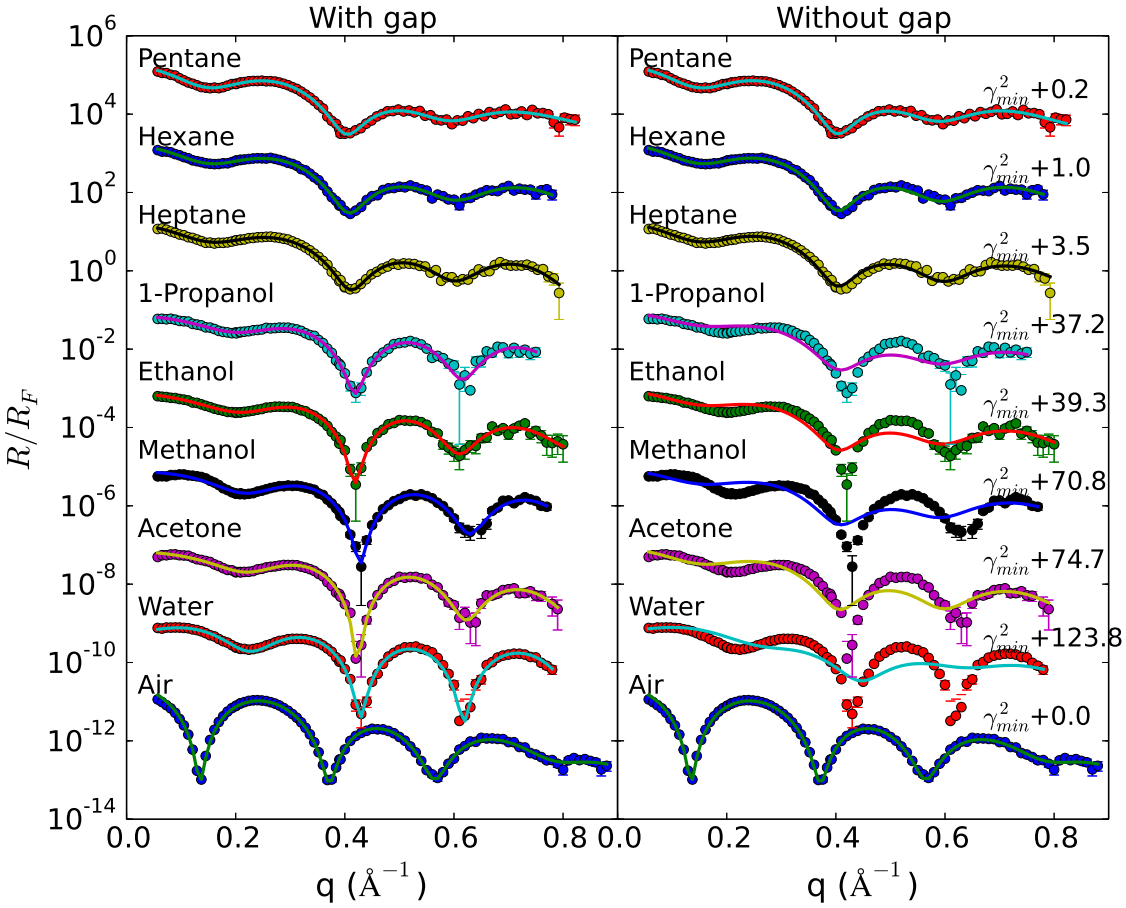

Figure 3.3. X-ray reflectivity data normalized to Fresnel reflectivity (solid circles) of OTS-solvent (air) interface. Left, solid lines are the best fits with gap. Right, solid lines are the best fits without a gap. The data and fit curves are shift by 2 orders for clarity. The increase of merit function by not using a gap is labeled at the end of each curve.

substrates are cut from the same wafer. The tilted OTS hydrocarbon chain can behave differently in air and solvents with different properties. This subtle change should be taken into consideration especially for studies that focus on angstroms length scale and very subtle change in the electron density contrast. Secondly, it's well known that the more parameters you have, the better the fitting will be. So, if one starts with the fixed

parameter for a dry film and fits the reflectivity curves with one more gap layer (with at least 3 more parameters), it's very likely to yield better fitting at some combinations of those additional parameters. Apart from the statistical error, some error sources including the beam uniformity and systemic errors are difficult to be evaluated[**10**]. A model with a limited number of variables can never fit each data point precisely, thus there is always room for improvement. In other words, it's possible that the '*internal stress*' within the dry film fitting that can produce some artificial effects when more parameters are used to fit the data with solvents. To overcome this problem, we allow the parameters that model dry OTS film to vary within a reasonable region to release the stress. This analysis, is more robust than fitting all dry OTS parameters. The result is plotted in Figure 3.4 with color blue, green and red corresponding approximately to 68.3%, 90.0% and 99.0%.

In Figure 3.4(a), there is no solvent for dry film, which is equivalent thus the $\rho_g = 0.0$. The fittings along $\rho_g = 0$ have same quality fitting goodness as shown in blue on the contour. Another blue region lies at D_g less than 4.0 Å, which is about the resolution limit in this q range, while the density can vary over a large range. The effect of this additional gap was compensated for by the rest of variables, resulting in good fitting. However, one can see a region with deeper blue which means the introduction of a gap could improve the fitting slightly.

When solvents were added, the reflectivity curves changed dramatically. All the minima of the dry OTS shifted to higher q range. Although the XRR data from different solvents seem to follow the same pattern, clear differences can be found. The reflectivity fringes at high-q range are more prominent for water and acetone than alcohols and

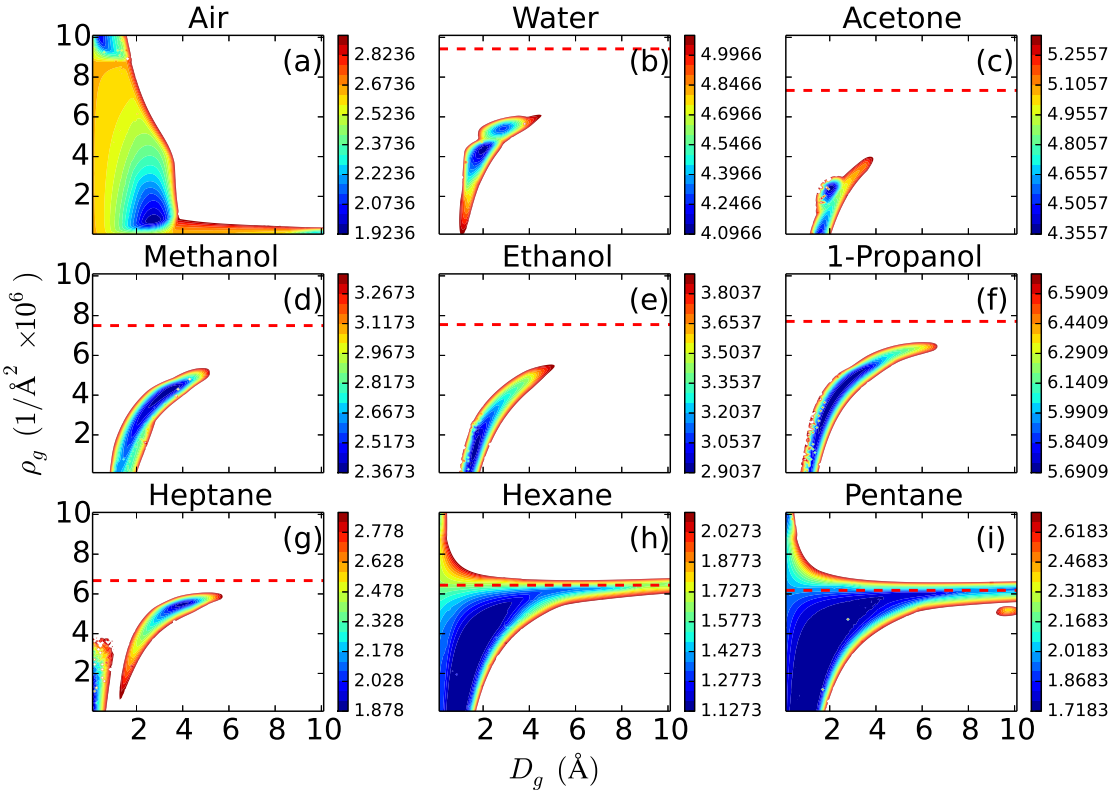

Figure 3.4. Contours of gamma square values on gap width-density plane for each solvent and air. The red dashed line in each graph corresponds to the density of that solvent. The yellow curves are the constant effective width curve.

the alkanes. The low-q XRR data also have a downward curve for water, acetone and methanol. The curvature decreases for ethanol and 1-propanol, before becoming negligible for the alkanes.

The contour plots for OTS with solvents in Figure 3.4 demonstrate the change of the gap from one solvent to another in a remarkable way. Water data indicates the gap can be 1.0-5.0 Å wide, depending on the choice of the gap density. The best fit is at $D_{\text{gap}} = 3.55$

Solvent	Water	Acetone	Methanol	Ethanol
Contact Angle	98.2/118	9.5	31.5	N/A
Surface tension (mJ/m^2)	72.4	25.2	22.6	22.8
Relative Polarity	1.000	0.355	0.762	0.654
Solvent	Propanol	Heptane	Hexane	Petane
Contact Angle	<10.0	<10.0	N/A	N/A
Surface tension (mJ/m^2)	23.3	20.1	17.9	15.5
Relative Polarity	0.617	0.012	0.009	0.009

Table 3.1. Summary of contact angle on OTS, surface tension and relative polarity for the solvents used in this study.

Å and 64.5% of bulk density, compared to $D_{\text{gap}} = 3.8$ Å and 71% of bulk density reported by Mezger et al[**21**]. This corresponding to an effective gap width of 1.2 Å, confirming the existence of a gap 20% larger than the methyl gap (yellow curve). This benchmark verifies our experimental setup and justifies our data analysis techniques.

XRR data from the interface of OTS and polar solvents, including acetone, methanol, ethanol and 1-propanol were also analyzed in the same way, shown in Figure 3.4 (c) (f). The contours for these solvents, similar in the overall structures as the one of water. The good-fit profiles lie in the curved blue stripes on the gap width-density plane, which represents non-zero gaps. For the alcohols, small variations on the contours can be founds. The blue region extends to larger width and the solvent density (the red dashed curve in each figure), as the hydrocarbon chain increased. For 1-propanol, the blue stripe follows

the constant effective width of methyl gap, indicating it's possible to explain that the gap is due to the methyl head group.

When the alcohol group is replaced by hydrocarbon, it's alkane (oil like) with negligible polarity. The non-polar solvents in this study, heptane, hexane, and pentane, changed the fitting contours drastically, as shown in Figure 3.4 (g)-(h). The good fitting region in the contour extends further and merges with the $\rho_{\text{gap}} = \rho_{\text{solvent}}$ line. In other words, the good fitting has to be either from gap density equals to the density of solvent, or the width of the gap is less than 3 Å. The upper limit of the effective width is about size of the methyl gap. The gap isn't mandatory to achieve a reasonable fitting from the data analyzing perspective. However, this doesn't say that no density depletion region exists for alkanes contacting OTS.

3.3.3. Discussion

Water, acetone, methanol and ethanol all have a large gap that cannot be explained by the methyl gap. For the non-polar alkanes, as well as 1-propanol, either the gap can be attributed to the methyl gap or the gap is too small to identify. Contact angle is usually used to monitor how the solvent interacts with the functionalized surfaces. All the solvents in this study (Table 1.), except for water, have < 90 degree contact angle with OTS SAM. Acetone, 1-pronol and alkanes with contact angles less than 10 degrees are actually very 'hydrophilic'. This indicates that the gap may not be a property that directly associates with the contact angle. The gap seems to originate from the competition between the intramolecular force in the solvent and the OTS-solvent interaction. Water, acetone and alcohols [**18**] are polar solvent due to the hydrogen bonding. Meanwhile,

the hydrocarbon chain of the alcohols and alkanes interact with other molecules as well as the OTS hydrocarbon surface. If the hydrogen-bonding is stronger than hydrocarbon affinity (water, acetone, methanol and ethanol), the solvent molecules are pulled from the surface to the bulk which creates the low density region that cannot be explained by the methyl gap. If the hydrocarbon affinity is stronger than the hydrogen bonding, as in 1-propanol and alkanes, a gap still exists but is mainly due to the methyl gap. It is worth noting that the intramolecular interaction doesn't necessarily have to be hydrogen-bonding. Electrostatic force in ionic liquids, for example, may also compete with the surface-solvent interaction.

The effective width for alkanes are less than or equal to the methyl gap, suggesting that there is no free space when those solvents contact OTS, or solvent molecules ordering on the OTS surface. The contour of heptane is slightly differently from the ones for hexane and pentane. The fitting without gap for heptane increased the merit function by 3.5 while this number for hexane and pentane are 1.0 and 0.2 respectively. This is probably due to that factor that heptane has the longest molecule making it unfavorable in entropy to align on a surface.

3.4. Conclusion

The perpendicular molecule distribution profiles at the interface of several common solvents and hydrophobic OTS SAM surfaces were studied with specular X-ray reflectivity. We mapped the contour of the surface electron density depletion layer (gap) and compared it to the gap caused by low density methyl group. Polar solvents, including water, acetone, methanol and ethanol were found to have a gap lager than the methyl gap.

However, 1-propanol and the non-polar alkanes including pentane, hexane and heptane contact the OTS film directly with negligible distance. A competing mechanism between intramolecular hydrogen-bonding in solvents and solvent-surface interaction is proposed to explain this phenomenon.

CHAPTER 4

X-ray Reflectivity Studies of Room Temperature Ionic Liquids at Charged Surfaces

4.1. Introduction

Room temperature ionic liquids (RTILs) are melting salts at or below room temperature. Unlike water and oil whose molecules are neutral, RTILs are made up of charged ions. The first RTIL discovered is Ethanolammonium nitrate in 1914 by Walden[**32**]. However, not until the 2000s when RTILs with high stability against moisture and temperature were discovered did the interest of research and development of RTILs start to grow dramatically[**33, 34, 35**]. RTILs differ from conventional electrolytes, including water, methanol and non-aqueous acetonitrile and toluene, in several ways.

RTILs are liquids without solvent, thus the charge density is very high. The typical value is 1.0M∼10.0M depending on the cation/anion size. This is comparable to high concentrated or saturated salt solution. Electrostatic interaction, accompanied by van der Waals force, steric interaction, hydrogen bonds.

First, the electrochemical window (EW) for RTILs can reach 4∼6V. In contrast, aqueous electrolytes only have a EW of 1.23V, a hard limit set the electrolysis voltage of water. The four times augment in EW makes a great difference when it comes to energy stored in capacitors, which is proportional to the voltage square.

Most RTILs have very low vapor pressure and high thermal stability. In fact, a common practice of purification RTILs is to put them in vacuum oven ($T = 373$K). This makes RTILs much safer for devices and applications that fire is strictly forbidden, for example, electric vehicles.

The cations of RTILs are usually organic. The properties of RTILs, including density, hydrophobicity, viscosity and melting temperature, can be tuned by using different cations, for example ones with longer/shorter hydrocarbon chains. Together with the various choice of anion, the combination of RTILs is almost infinite. It gives RTILs unique advantages for applications where a particular property is desirable.

These unique properties of RTILs make them great candidates for applications, including energy storage (battery and supercapacitor), catalysis and organic synthesis, electrodeposition, lubrication, separation and analysis, CO_2 absorption *et al.*

The scope of this Thesis is limited to the organization of anion/cation of RTILs at charged surface, and the time scale associated with the process.

4.2. Background

Gouy-Chapman-Stern (GCS) model is successful in describing the distribution of diluted ions/charged nano-particles near electrode[**36**], and was confirmed by X-ray standing wave studies [**37**]. For a plane surface in contact with electrolyte, Gauss's law requires

$$\nabla^2\Phi(z) = \frac{-1}{\epsilon_0\epsilon_r}(q_+c_+ - q_-c_-) \tag{4.1}$$

in which $\epsilon_0 = 8.854 \times 10^{-12}\mathrm{Fm}^{-1}$, the vacuum permittivity. ϵ_r is the relative permittivity. $q_\pm$ and $c_\pm$ are the unit charge and concentration of cation/anion. $q_+ = q_- = e$ for RTILs.

Under mean-filed assumption, the anions/cations are in thermodynamic equilibrium, described by Boltzmann distribution,

$$c_+ = c_+^0 \exp\left(-\frac{q_+\Phi(z)}{k_B T}\right) \qquad c_- = c_-^0 \exp\left(\frac{q_-\Phi(z)}{k_B T}\right) \tag{4.2}$$

$c_\pm^0$ are the concentration in the bulk. $c_+^0 = c_-^0 = c^0$ as is required for charge balance. Expand the exponential terms to the first order,

$$\nabla^2\Phi(z) = \frac{2e^2c^0}{\epsilon_0\epsilon_r k_B T}\Phi(z) = \frac{\Phi(z)}{l_D^2}, \qquad l_D = \sqrt{\frac{\epsilon_0\epsilon_r k_B T}{2e^2c^0}} \tag{4.3}$$

$$\Phi(z) = \Phi_0 \exp(-z/l_D) \tag{4.4}$$

Plug in the typical values for RTILs, $c^0 = 10^{27}\mathrm{m}^{-3}$, $\epsilon_r = 10$, the Debye length at room temperature is $l_D = 0.84$ Å, which is much smaller than the size of anion/cation (~ 10Å). Apparently GCS model doesn't work for RTILs which have strong ion-ion interactions due to the high ion concentrations. Differential capacitance studies of RTILs-electrode interface revealed behaviors that depends on the electrode type, frequency, applied potential, RTIL species etc. The differential capacitance/potential curves are camel-shaped with one minimum which cannot be explained by GCS capacitance [**38, 39, 40, 35**]. This behavior must originate from the nano-structure of RTILs near electrode surface, but what that structure is and how it responds to the applied potential are poorly understood.

To study the nano-structure normal to an RTIL-electrode with controlled potential, the experiment techniques have to be in-situ and non-destructive. X-ray and neutron reflectivity are two such tools. With the advantage of tuning the scattering length density by deuterating RTILs, neutron reflectivity (NR) was employed to study RTILs-solid interface[**41, 42**]. However, NR has much lower flux than synchrotron X-rays, which often reduces NR's resolution. X-rays are only sensitive to the total electron density (assuming X-ray energy is much higher than the absorption edges of elements in RTILs). In order to distinguish the cation and anion, the RTILs have to possess high electron density contrast between anions and cations.

There have been several previous studies of RTIL structure near solid surfaces[**43**] [**44**] [**45**] [**46**], where there is no applied voltage and no way to measure the surface charge in situ. In refs [**44**] and [**43**], the reflectivity data for an RTIL on insulating sapphire substrates, assumed to be charged due to X-ray exposure, were fitted with distorted crystal model with alternation cation/anion layers. However, in ref [**45**] similar layering was reported using uncharged (hydroxylated) sapphire. Thus, Uysal et al. [**47**] have correctly noted that the observed layering may have the same origin as that seen even in nonionic molecular liquids [**8**]. Reference [**46**] reported a dense layer at a presumably uncharged graphene surface, but alternating cation and anion layers at a presumably charged mica surface.

There have also been two prior X-ray studies of RTIL structure using applied voltages at conducting substrates (electrodes). Yamamoto and coworkers [**48**] used a gold electrode and compared the X-ray reflectivity data at ± 1.5 V and ± 3.0V (no reference electrode was used thus the effective potential drop of the RTIL interfacial structure couldn't be

determined). The differences were slight. Although the reflectivities were monotonic (no interference maxima or minima), the data were fitted using a distorted crystal model (implying layering at the interface). Uysal et al[**47**] used epitaxial graphene on SiC wafers as the electrode, and also reported alternating anion/cation layers in the interfacial RTIL at the largest positive (+1.0V vs. Pt wire) and negative voltages (−0.4V vs. Pt wire) studied.

Experiments using force measurements, the only other applicable technique with comparable spatial resolution normal to the interface, also reach a variety of conclusions. Atomic Force Microscopy data indicate layered structures near gold electrodes[**49**] and pyrolytic graphite [**50**], with the number of layers increasing as a function of applied voltage. However, measurements using a Surface Force Apparatus[**51**][**52**], which can be thought of as replacing the AFM tip with an essentially flat mica surface, indicate the presence of an adsorbed ion layer followed by a monotonic diffuse distribution, consistent with the GCS model.

Our X-ray reflectivity study (see schematic diagram, Fig. 4.1) departs from previous studies in several crucial ways. First, since gold has an extremely high electron density (4.40 electrons/Å^3, over an order of magnitude greater than typical ionic liquids); the x-ray reflection from gold[**48**] swamps the reflection from RTIL interfacial structures of interest. We used H-terminated silicon substrates instead; silicon has an electron density of 0.70 electrons/Å^3, only about twice that of the typical RTIL. We show that a given interfacial structure will lead to visible interference features in the X-ray reflectivity if

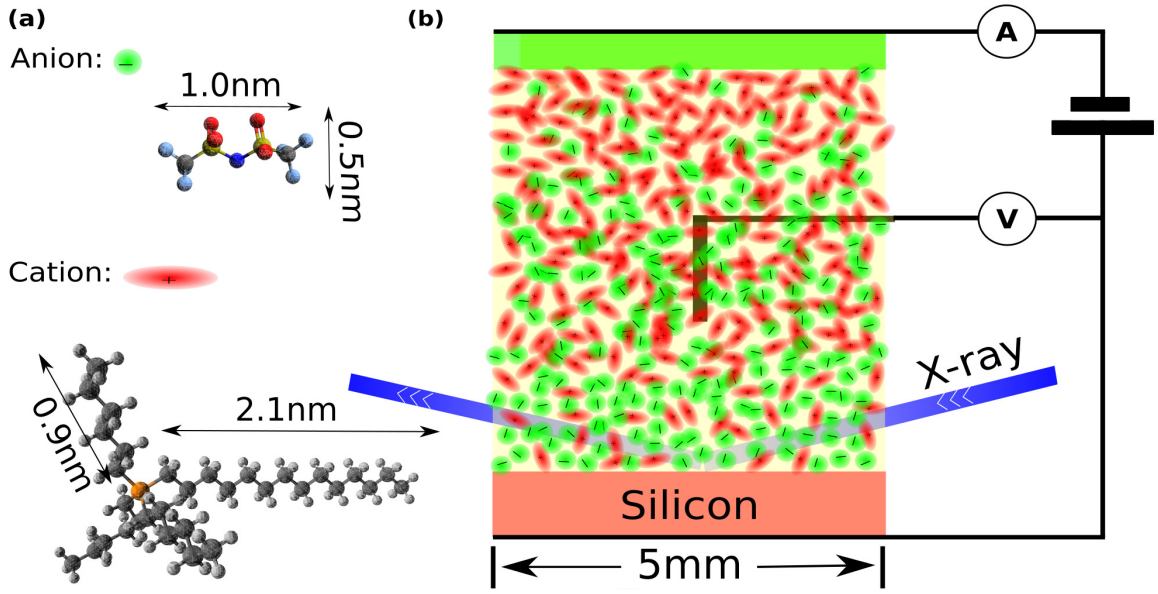

Figure 4.1. (a) The dimensions and molecular structures of anion and cation used in our experiment. Atoms are represented by colors as follows: Red=O, dark blue=N, yellow=F, light blue =S, orange=P, black=C, gray=H. Black and gray spheres are C and H atoms. (b) Schematic diagram of the experiment, showing the grazing incidence X-ray geometry (angle of incidence exaggerated).

the substrate is silicon, but not if it is gold. Second, we used an RTIL that had a wide electrochemical window, allowing us to apply higher voltages. Third and most important, we performed a detailed study as a function of voltage, rather than one or two voltages as in the previous studies[**48**][**47**][**53**]. This allowed us to observe clear trends in the interfacial structure as a function of the applied voltage. Our result differ substantially from those reported in ref [**47**][**53**], but note that the cation of RTIL in this study is different.

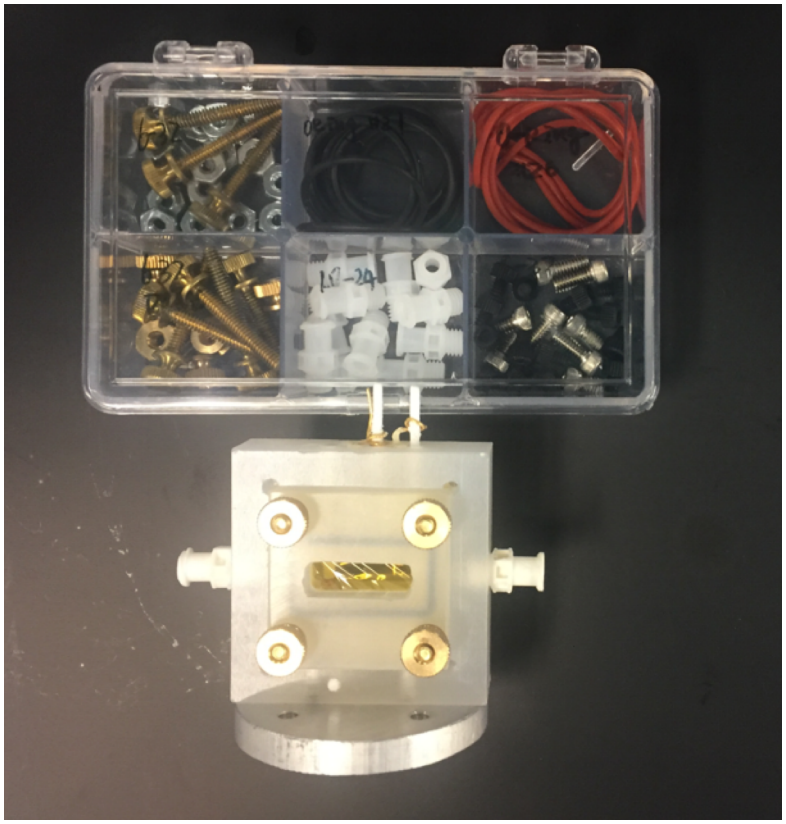

Figure 4.2. The assembled in-situ transmission cell used in this study. The details are described in the text.

4.3. Experiment details

Several RTILs were used in this study, including [TDTHP][NTF_2] (99% purchased from Iolitec and 95% purchased from Stem, with no obvious difference in data), [TDTHP][Cl] (95% purchased from Sigma), [MTOA][NTF_2] and [TMOA][NTF_2] (both 99% purchased from Iolitec). The chemicals are dried in vacuum oven at 100 Celsius degrees for 2-3 days. [TDTHP][Cl] was dried at room temperature because it changed color when heated, presumably due to some unstable impurities. Silicon chips were purchased from Tedpella. They are p-doped with resistance of 1-30 cm, diced into 7mm by 5mm. The chips are treated with rapid thermal process (RTP, NUFAB) at 1100 degree for 5 mins, resulting a

460 angstrom thermal oxide layer. After oxidation, chips are cleaned in Piranha solution (Sulfuric acid: Hydrogen peroxide, 7:3, volume ratio, extremely violent) for 30mins to remove residues. They are rinsed with copious of ultrapure water before stored in water. Before each experiment, the chip is immersed into BOE solution (Danger, AF875-125, HF%=6.3%, NH4F%=34.8, purchased from Sigma) for about 100s. Then, it is rinsed with copious of water and dried with ultrapure Nitrogen.

The transmission sample cell and the covers are made of Kel-F, for maximal chemical and moisture resistivity. The cavity for the RTIL, chip and electrodes has dimension of 6mm by 6mm by 20mm and volume of 0.70mL. Gold wires are used as contour electrodes, pseudo reference electrode, as well as leads to connect the silicon chip (working electrode). The electrodes are connected to the terminals outside of the cell through tiny holes (0.0021 inch) are drilled on the body. Gold wires (0.0020inch) covered with fresh prepared Tor-seal resin are inserted to the holes (1day is allowed for the solidification). No leakage in the holes are found during experiment. Silicon chip is mounted to the cell with a disposable Nylon set screw. Before each experiment, the electrical conductivity is confirmed by measuring the resistance using a multimeter. Kapton films, cleaned with sonication in acetone, are used as the X-ray windows. The covers with O-rings are pressed against the Kapton film to the cell body with four thumb screws. Nitrogen flushes for 30s to remove the airborne impurities during cell assembly. About 1.2mL RTIL is injected into the cell using a disposable syringe, leaving no visible bubbles. Although the thin film cell would reduce the attenuation of photons through RTILs bulk[**54, 48**], such setup was not used because of the high resistivity of RTILs and the resulting risk of nonuniform interfacial

potential. The potential is controlled by a potentiostat (DY2311), with gold wire as pseudo reference electrode and contour electrode, silicon chip as the working electrode.

Specular X-ray reflectivity measurements are performed at Sector 12BM-B and 33BM-C at Advanced Photon Source (APS), Argonne National Lab. The energy of the synchrotron x-ray is at 19 KeV, which penetrates the 5mm transmission cell with acceptable attenuation. The beam is focused to be 0.5mm by 0.5mm, at a flux of about $10^{10} \sim 10^{11}-$ photons/s. The signal and noise are collected simultaneously with Pilatus 100K area detector, which is located about 70cm after the sample.

XRR data are corrected for filter transmission, foot-print, background subtraction, and beam flux.

4.4. Result and analysis

4.4.1. Formation of crowding layer

The RTIL studied was trihexyltetradecylphosphonium bis(trifluoromethylsulfonyl)imide ([TDTHP][NTF_2]) , see Fig. 4.1. Fig.4.3 shows a cyclic voltammogram obtained using our experimental setup. The electrochemical window (EW), within which it is assumed that there is no electrolysis, is typically defined as the voltage range in which the current is less than $0.1 \sim 1.0 mA/cm^2$ The ions in our IL, [TDTHP] and [NTF_2], have some of the largest electrochemical-window potentials among common IL anions and cations $-3.64V$ and $+2.70V$ respectively; Fig. 2 is consistent with these numbers.

As previously noted, X-ray reflectivity is sensitive to the total electron density, including all electrons in each atom. In the RTIL studied, there is a significant difference

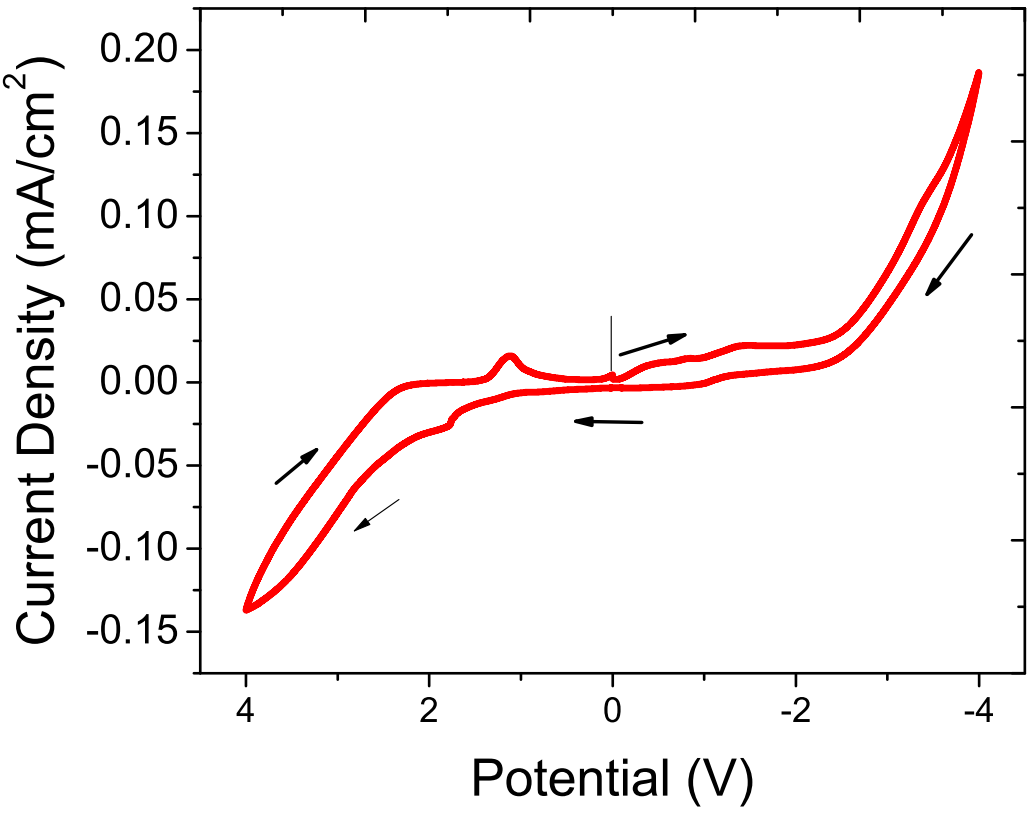

Figure 4.3. Cyclic voltammogram for [TDTHP][NTF_2] measured in our experimental setup, i.e. with Si and Au electrodes.The vertical line and arrows indicate the starting point and scan direction.

between the sizes and electron densities of the anion and cation. The bulk RTIL has electron density $\rho_{\mathrm{IL}} = 0.347$ electrons/Å^3. The cation is large (950Å^3) and has only slightly lower density than the bulk liquid (0.289 electrons/Å^3), while the anion is small (0.24 Å^3) and is much denser than the bulk (0.577 electrons/Å^3). (See Supplementary Information for a table showing the numbers from which the electron densities were calculated.) The difference in electron density allows us to interpret any deviations from the bulk RTIL electron density as due to an imbalance between cations and anions, and thus to calculate

the charge density. Specifically, assuming the cation(anion) carries charge of Q(-Q), the charge density ρ_c can be calculated from

$$\rho_c = Q(\rho_s - \rho_{\mathrm{IL}})\frac{V_a + V_c}{V_a N_C - V_c N_a} \tag{4.5}$$

where ρ_s and ρ_{IL} are the electron density at the interface and the average electron density of the bulk ionic liquid. $V_a(V_c)$ and $N_a(N_c)$ are the effective volume of and the number of electrons in, on anion (cation). Note that this euqation does not allow for compression at the interface (which would change V_a and/or V_c) and assumes that the ions do not have fractional charge.

The etched silicon (111) surface can undergo surface reconstruction[**55**], leading to a relatively rough surface which causes interfacial reflectivity data to drop rapidly with increasing q. Flux attenuation during transmission through the bulk RTIL, and scattering background from bulk IL (which has a broad peak around 0.41), further reduce the highest momentum transfer in a reflectivity scan to 0.30Å^{-1}, corresponding to a spatial resolution function of width $\pi/q_{\max} \sim 10.0$Å. Fig. 4.4 shows X-ray reflectivity data R divided by the ideal Fresnel reflectivity R_F, as a function of applied voltage (measured between the Si substrate and the reference electrode). At negative voltages (Si electrode at negative potential relative to the reference electrode), the reflectivity curves have no prominent features. This is because of the poor density contrast between the bulk liquid and the cations that are presumably attracted to the electrode surface, as shown in Fig. 4.5. A model with multiple parameters can be proposed to fit the data, however, the result will not be robust.

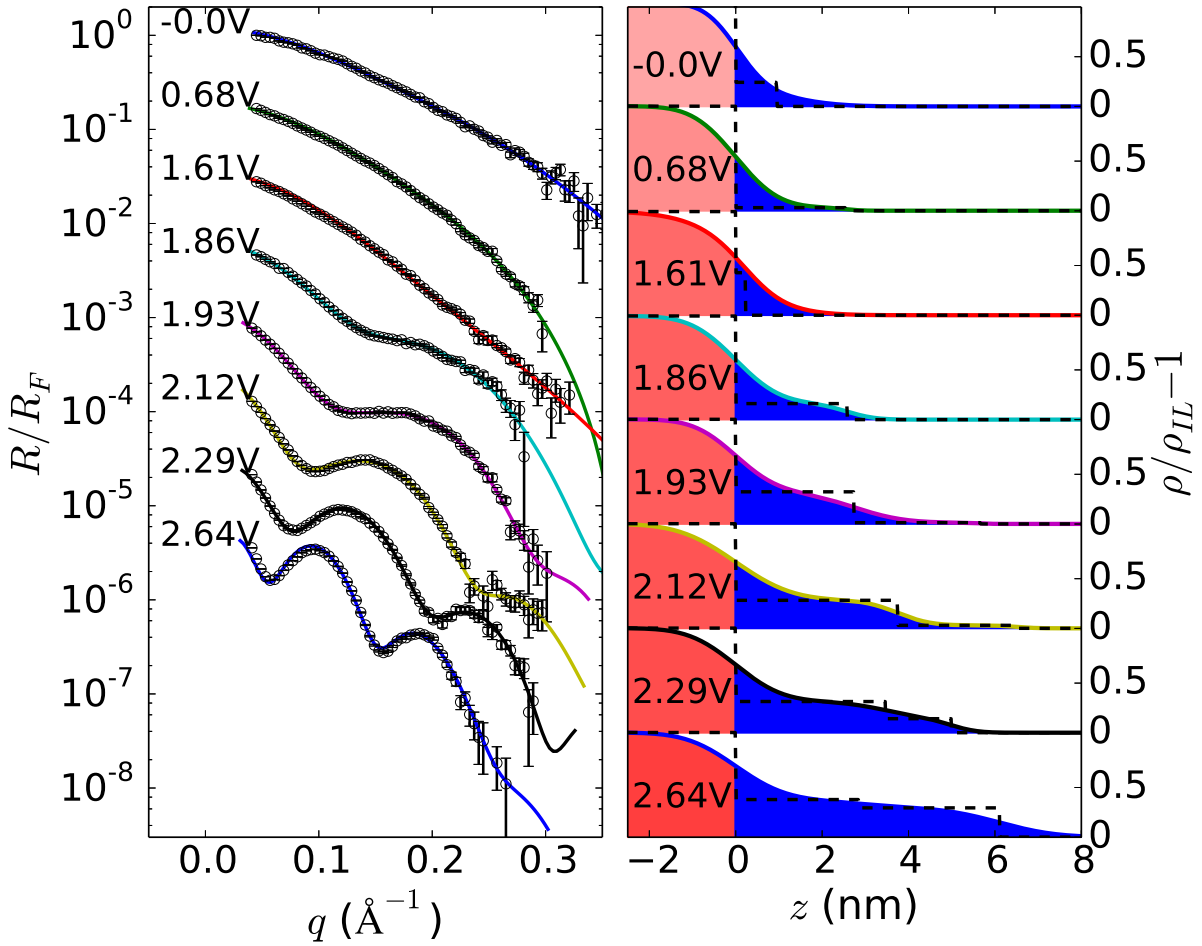

Figure 4.4. Left: voltage dependent x-ray reflectivity data (open circles) and fits using the slab model discussed in the text (solid lines). The curves are shifted vertically relative to each other for clarity. Right: the voltage-dependent electron density enhancement profiles, $(\rho(z)-\rho_{\mathrm{IL}})/\rho_{\mathrm{IL}}$ where ρ_{IL} is the bulk liquid density, obtained from slab model fits to the data. The dashed lines show the slabs without interface broadening (roughness); the smooth curves show the roughness-broadened profiles. Red=Si electrode; Blue=anions.

For positive voltages, the reflectivity curves are featureless at low voltages. Featureless curves can still be (and often are) fitted with postulated models, but the conclusions are

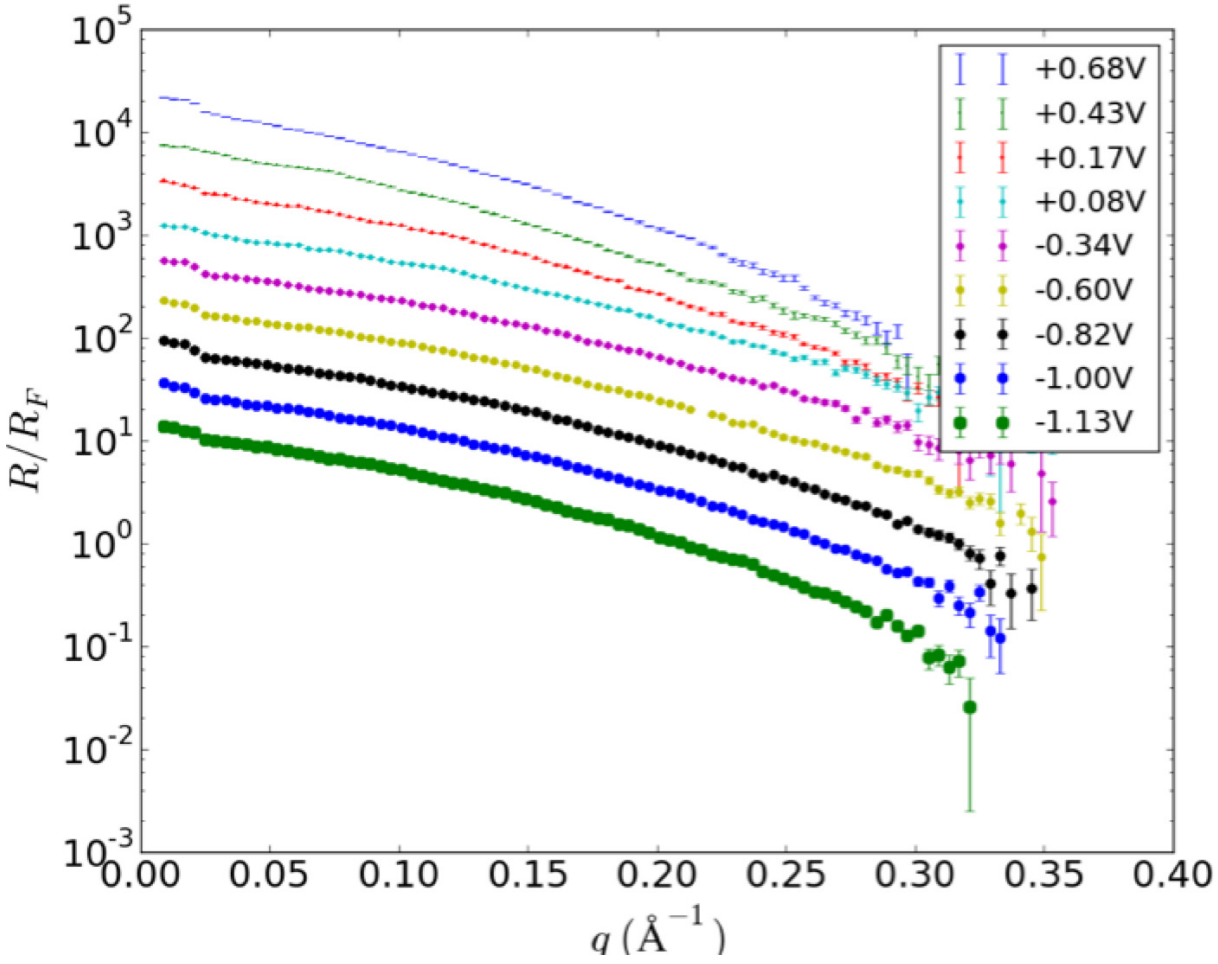

Figure 4.5. The reflectivity curves at negative potentials and low positive potential.

not robust. However, at higher voltages, oscillations begin to appear, and the minima shift to lower q as the applied voltage increases. Such oscillatory features allow more definitive fits to the data. At each voltage, it takes about 20 mins for the reflectivity curve to become stable, i.e. for the interfacial structure to form. The data are then stable over a period of at least 40 mins, showing that they are not electrolysis products collecting with time.

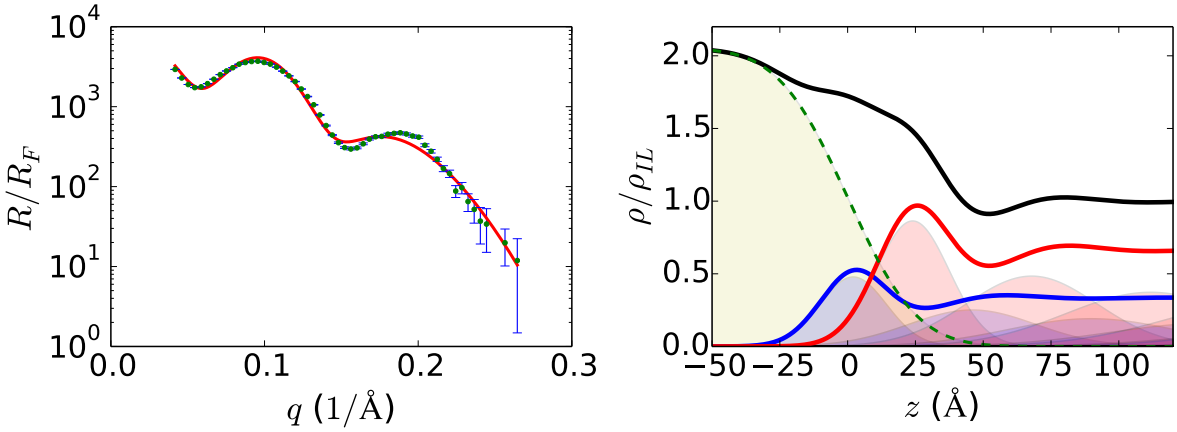

Figure 4.6. The left panel is XRR data (solid green circles) and the best fit with distorted crystal model (red curve). The right panel shows the fitted electron density profile. The dashed green, red and blue lines are profiles of the silicon electrode, cation and anion respectively. The black curve is the total electron density.

The general procedures for fitting X-ray reflectivity data have been discussed elsewhere. Here we address the choice of model to fit the data. In many previous studies[**43, 48, 56**], a distorted crystal model has been used to fit the data. In this model as applied to an ionic liquid, there are alternating layers of cations and anions, with each layer having the same charge but becoming increasingly diffuse (broad) until the structure becomes that of the bulk liquid. This might happen if there is overcharging—the first layer of anions carries more charge than necessary, which requires a subsequent layer of anions, resulting in charge oscillations decaying into the bulk liquid. When there are maxima and minima in the reflectivity, a simple slab model (interfacial steps of variable width, density and interface roughness) will also fit the data.

In Figure 4.6, the distorted crystal model is used to fit XRR data at 2.64V, with considerable deviation.The best-fit roughness of the silicon surface comes out to be 2.0nm, a very high value, and this is because the fit is trying to account for the interfacial anion layer even though the model does not include such a layer.

only if the Si surface has a very large roughness (> 20.0Å), and this indicates that there is a dense interfacial layer that the distorted crystal model by itself cannot capture. The authors of Ref.[**47**] have also found that the distorted crystal model must be supplemented with an interfacial slab to fit the data from a similar system. Further, since our data were collected at multiple voltages and show the reflectivity minimum moving to smaller q with increasing voltage, the thickness of every layer in the alternating-layer picture would have to increase with voltage, which is counterintuitive and not theoretically predicted. We are able to fit our data with interfacial slabs, without adding alternating anion-cation layers. Of course, a slab model is also an approximation to reality; it is a 'pixelated' representation of the actual density profile, taking into account the finite spatial resolution of the reflectivity technique.

As shown in Fig.4.4, the reflectivity curve is featureless at and below 1.61v, but develops oscillatory features (fringes) above that voltage. We fitted all data using either one or two slabs, but when there are no features, the fits do not give significant results (error bars include zero.) Up to 2.12 volts, the data can be fitted using just one interfacial slab. The data at higher voltages can also be fitted with one slab, but the fit is slightly improved by using two adjacent slabs. This suggests that the actual electron density profile is rounded such that two 'pixels' represent the actual profile better than one uniform-density slab

can; however, the basic features of the interfacial region (total thickness, average density) remain essentially the same whether a one-slab or two-slab fit is used.

The fitting parameters are tabulated in the Supplementary Information, and Fig. 4 shows the slab thickness (total thickness if two slabs), electron density enhancement (average enhancement if two slabs), and calculated surface charge density as functions of voltage. The qualitative trends are as follows. For lower voltages, when the reflectivity has no oscillatory features, the error bars are large and include zero. At higher voltages the interfacial density is higher than the bulk density, and this means that there is an excess of anions over cations, as one would expect. The average electron density varies only weakly with voltage, and never reaches the density of the anion. At most the interfacial layer averages 80% anions, 20% cations (this is the number ratio; in terms of volume it is 60% anions, 40% cations). This layer is not a monolayer; rather, above a threshold voltage $V_{\rm off} = 1.75$V the slab thickness W increases rapidly with voltage until it is ~ 60Å, much larger than the anion dimensions.

These data are consistent with the formation of a crowded layer above a threshold voltage, as predicted in Ref[**57**] but never before observed, with the thickness being a strong function of the applied voltage. Since the lower-voltage data show no fringes, there is no significant evidence of any interfacial structure below the threshold. Nonetheless, the existence of a threshold voltage requires explanation. It is possible that for $V < V_{\rm off}$, the interfacial electric field is balanced out either by weak alternating layers of cations and anions, or by a diffuse Gouy-Chapman double layer as in ionic solutions. However, any such structures would have to be too weak to have an identifiable signature in the x-ray reflectivity.

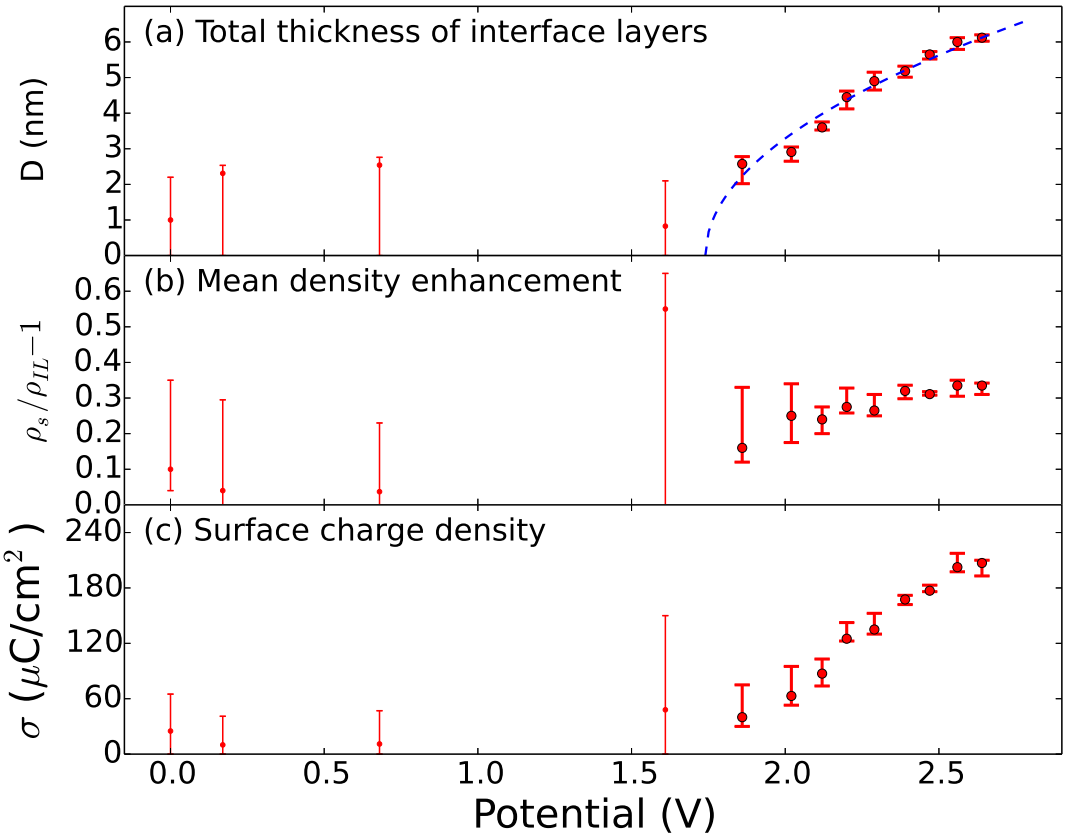

Figure 4.7. Best-fit parameters as a function of voltage. (a) Slab width (for one slab fits) or total width of interface slabs (for 2-slab fits) (b). The interfacial slab density enhancement $(\rho(z)-\rho_{\mathrm{IL}})/\rho_{\mathrm{IL}}$ where ρ_{IL} is the bulk liquid density (mean enhancement is shown for 2-slab fits). (c) Surface charge density (anionic charge per unit area) calculated from the slab electron density.

If there is a potential difference VV_{off} across an uniform charged slab of thickness W, where V_{off} is an offset voltage, Gauss's Law applied to a charged slab requires that $W^2 = (\epsilon_0\epsilon_r/\rho_c)(V - V_{\mathrm{off}})$ where ρ_c is the charge per unit volume. Fig. 4.7(b) shows that the electron density of the slab is at most weakly V-dependent; we ignore this weak

dependence and assume that the slab electron density ρ_s and therefore the charge density ρ_c do not depend on V. With this assumption, $W = \lambda\sqrt{V - V_{\text{off}}}$ where λ is a constant. The dashed line in Fig. 4.7(a) shows the best fit to this functional form. Clearly the data are quite consistent with the predicted V-dependence. This fit gives us $V_{\text{off}} = 1.75$V and $\lambda = 64.5\text{ÅV}^{-0.5}$.

Two significant anomalies must be noted. First, as previously noted, we can calculate the charge density ρ_c within the slab from the electron density data in Fig. 4.7(b): at 2.64V we find that $\rho_c = 9.3 \times 10^{-19}$ Coulombs/nm3. Using this value and the typical range of ϵ_r for bulk RTILs ($\sim 15 - 20$), the calculated constant of proportionality $\lambda = \sqrt{\epsilon_0\epsilon_r/\rho_c} = 0.40\text{ÅV}^{-0.5}$, much smaller than the value of 6.45 obtained by fitting the D-V curve. Second, using the surface charge density the slope of the σ_V curve in Fig 4(c), we estimate the differential capacitance per unit area to be $> 200\mu\text{F/cm}^2$. However, at 100Hz we have measured the AC capacitance per unit area to be $20\mu\text{F/cm}^2$. The latter value is in the normal range reported for RTILs, whereas the capacitance calculated from X-ray data is an order of magnitude larger.

The conversion factor from electron density to charge density changes if in fact the ions have only fractional charge. In the bulk RTIL, it has been suggested that the actual ionic charges are $\sim 0.6 - 0.8$ electrons/ion[**58, 59, 60, 61**]. This is not small enough to explain the observed order-of-magnitude discrepancy. On the other hand, it is known that RTIL interfacial capacitance depends on frequency as $\omega^{-\alpha}$ where $\alpha \sim 0.1 - 0.3$, which would diverge in the DC [**39**]. This suggests that the DC capacitance of electrode-RTIL interfaces, which is not so easily measured, may in fact be very large, while much lower values are reported using AC measurements. The source of such a difference would be the

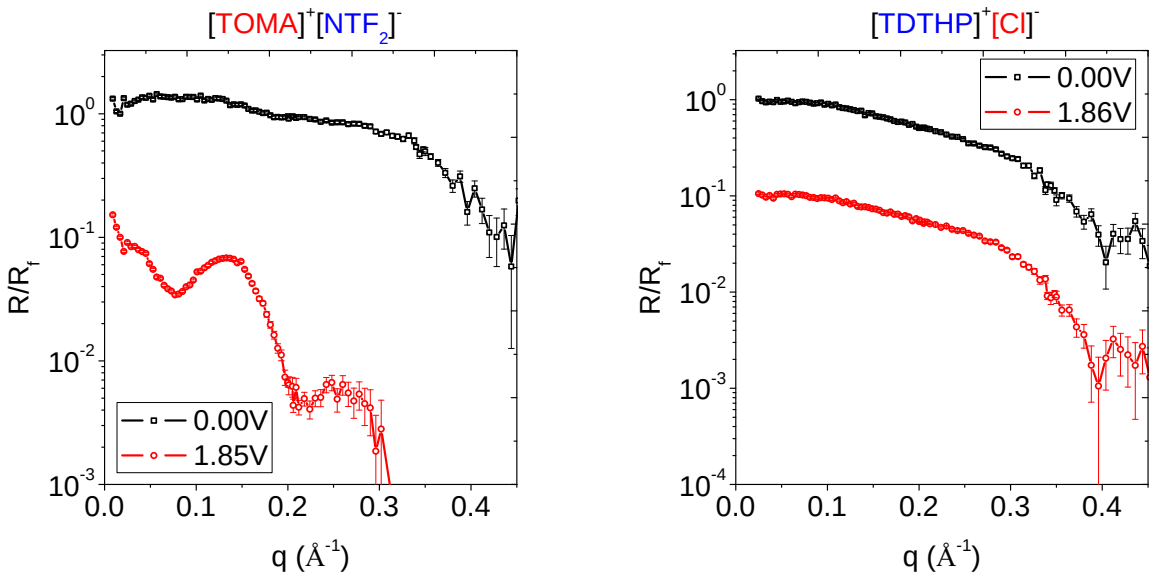

Figure 4.8. Control experiments with (a) $[TOMA]^{+}[NTF_2]^{-}$ (same anion) and (b) $[TDTHP]^{+}[Cl]^{-}$ (same cation). The black and red curves are XRR curve at zero voltage and positive voltages respectively.

known low mobility of RTIL ions. The anomaly may indicate that the permittivity of the interfacial layer is very different from the measured permittivity of the bulk—certainly there is no reason why they should be the same. Unfortunately, there is no experimental probe at present that directly measures either the effective charge per anion or cation in, or the permittivity of, a nanoscale interfacial layer.

We have performed control experiments with several other RTILs, shown in Fig. 4.8. $[TOMA]^{+}[NTF_2]^{-}$, which has the same anion but a different cation, showed qualitatively similar behavior to that reported above, while $[TDTHP]^{+}[Cl]^{-}$, which has the same cation but a different anion, gave a null result, This is reasonable: a Cl- anion carries only 17 electrons while $[NTF_2]^{-}$ carries 138 electrons, so that for the same amount of

interfacial change, the chloride anion would create a much smaller interfacial electron density enhancement. Another RTIL, [N4111] $^{+}$ [NTF_2] $^{-}$ also demonstrated similar XRR pattern at high voltage, shown in Fig 4.8. The explicit dependence on voltage for these RTILs were not fully studied due to the limited beam-time. However, differences of the offset voltages and proportional constants are expected due to the cations. This also shows that the interfacial layer must be attributed to the dense [NTF_2] $^{-}$ anion, and not to spurious effects such as electrolysis products.

4.5. Conclusion

Our results provide direct confirmation of the prediction that there will be a thick "crowded" layer of ions near an electrode interface at higher voltages[**57**]. This layer develops only above a threshold voltage V_{off}. Counterintuitively, the crowded layer is not purely anionic, but at most $\sim 80\%$ anions and 20% cations. We see no evidence of either alternating layers of anions and cations ('overcharging') or a diffuse layer, although the existence of an offset voltage means that there could be interfacial structures too weak to detect. Further, our data suggest that the DC differential capacitance is much larger than typical values reported in AC capacitance measurements, and the permittivity of the interfacial layer is also very large. Both these possibilities have significant implications for the use of RTILs for energy storage and in electrochemical devices, and illustrate the complexity and novelty of this class of liquid electrolytes.

CHAPTER 5

Ultra-Slow dynamics in ionic liquids revealed by X-ray reflectivity

5.1. Introduction

The next generation of electrochemical energy storage devices, including batteries and supercapacitors, will ideally require not only high energy density but also high power density and fast charging rate[**62**]. Room temperature ionic liquids (RTILs) have been considered as novel electrolytes for such applications, due to their high charge density, wide electrochemical windows (5V wide compared to 1.23V for water)[**63, 64**], high thermal stability, low flammability and non-volatility. However, they are handicapped by their slow dynamics, including high viscosity, low electrical conductivity and small diffusion coefficient[**35, 65**]. An understanding of the nanoscale factors leading to these slow processes may lead to ways of selecting or designing molecular ions to optimize the electrochemical behavior of RTILs.

A number of theoretical papers have addressed the origins of the observed slow dynamics [**66, 67, 68, 69**]. An obvious timescale is $\tau_c = RC$, which is the governing timescale when the charge carriers can move rapidly. However, this timescale does not generally fit the observed response, and in those cases the limiting factor is the motion of ions within the RTIL. It is not clear how these should be described; for example, are there only local rearrangements of the ions, or do ions travel over distances comparable to the size of the

electrochemical cell? Several theoretical predictions will be discussed and compared to our experimental data later in this paper.

A number of research groups have recently studied aspects of the slow dynamics in RTILs. Uysal and coworkers performed an X-ray reflectivity study on a $[C9mim]^+[NTF_2]^-$ -graphene interface[**47, 53**], and discovered two processes associated with double layer formation, with time constant of 1s and 10s respectively. Both of these are much longer than the RC constant. Roling and coworkers studied the $[BMPyrr]^+[FAP]^-$ -gold (111) electrode interface with electrochemical impedance spectroscopy. The complex capacitance plot shows two distinct arcs with frequency of 1MHz-20Hz and 20Hz 0.1Hz[**70**]. The fast process is of the order of RC, while the slow process is order of 1s. Similar results were also reported in $[Py1,4]^+[FAP]^-$ and $[EMIM]^+$ $[FAP]^-$[**71**]. Nishi and coworkers studied the $[TOMA]^+[C4C4N]^-$ -gold interface with surface plasmon resonance (SPR)[**72**]. When a potential was applied to the gold electrode, the SPR signal took 100s to stabilize. They also found that the response to increasing and decreasing the potential had slightly different time scales, which was attributed to the asymmetrical anion/cation. During our previous study[**73**], we noticed that the crowded layer of anions took time to form, but once formed the layer was stable. The data we reported were for the time-independent state, collected at least 1200 sec after a voltage was applied or changed.

The large deviations between RC for the electrochemical system and the reported time scales confirms that the RTIL-electrode system cannot be simply treated like a traditional electric double-layer. Instead, its response to electric fields involves complex dynamics that requires careful study. However, measurements such as capacitance or SPR, while detecting time dependence, do not identify the nanoscale origins of the time dependence.

In the present study, we measured the time dependence of the 'crowded' RTIL layer near an electrode surface. Since the crowded layer is composed largely of anions, we directly observed the time-dependent response of anions independently of other dynamic processes in these systems.

5.2. Background

To study the charging process of ionic liquid capacitor, we start with the most simplified resister-capacitor (RC) circuit. When a the circuit is connected to a power source with voltage of U_0, the potential on the capacitor $\phi(t)$ follows the differential equation and initial condition,

$$R\frac{d(C\phi)}{dt} + \phi = U_0, \qquad \phi(t=0) = 0 \tag{5.1}$$

The solution is $\phi(t) = U_0[1 - \exp(-t/RC)]$, with charging constant of $\tau_c = RC$. For an electrochemical cell, because the resistance is inversely proportional to the cell area while the capacitance is proportional to the area, the RC constant is independent of the surface area. For a cell with unit area, the resistance is,

$$R = \frac{V}{J} = \frac{LE_0}{\mu E_0 \sum_{\pm} c_i q_i^2} = \frac{L}{\mu \sum_{\pm} c_i q_i^2} \tag{5.2}$$

V, J, E_0 and μ are the potential difference, current density, electrical field and ion mobility. $c_{\pm}$ and $q_{\pm}$ are cation(anion) concentration and charge per particle. Plug in the Debye length $\lambda_d = \sqrt{\epsilon_0 \epsilon_r k_B T / \sum_{\pm} c_i q_i^2}$ and Einstein relation, $D = \mu k_B T$ which bridges the ion

mobility with its diffusion constant D,

$$R = \frac{L\lambda_D^2}{D\epsilon_0\epsilon_r} \tag{5.3}$$

While the nature and origin of double layer capacitance in ionic liquids are under debate, the order of its capacitance can still be estimated as λ_D is $C_d = \epsilon_0\epsilon_r/\lambda_D$. Thus the RC time constant for the RTIL-electrochemical cell is,

$$\tau_c = RC = \frac{L\lambda_D}{D} \tag{5.4}$$

τ_c is considered as the primary time scale in RTILs. Apart from τ_c, that are two other time constants should be considered. When RTILs contact a surface that isn't so "charged", the local re-organization of anion/cation is capable to screen the charge. This process takes no longer than $\tau_D = \lambda_D^2/D$, or the time for ions to diffuse a distance of λ_D.

If the surface is highly charged, or connected to an external power source, it may require the cation/anion in RTILs to reorganize at a length scale of the electrochemical cell. In this case, ions are required to diffuse across the cell which takes $\tau_L = L^2/D$. It can be easily verified that that τ_c is the geometric average of τ_D and τ_L.

5.3. Experimental Details

The experiment setup is basically the same one used in the previous section. However, the measurement procedure has been optimized to detect the dynamic response of the structure of RTIL under external potential. Continuous reflectivity scans are taken before and after changing voltage. Each scan takes about 300 seconds, however the time resolution is much better than that. This is because the reflectivity decays so fast that

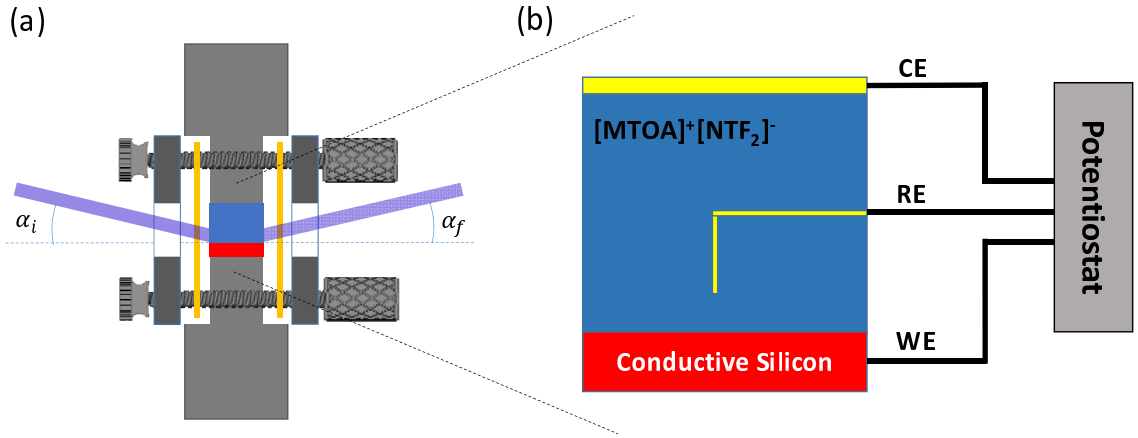

Figure 5.1. (a) Schematic diagram of the transmission cell used in this study. The cell body and window frames are made of Kel-F. The two yellow films are Kapton windows. The air-tight seal is achieved by pressing the frames with o-rings against the cell body. (b) A schematic diagram of the experimental geometry. The conductive silicon (red) is the working electrode while gold wires (yellow) are the counter-electrode and pseudo-reference electrode. X-rays are reflected from the slicon-RTIL interface.

much of the time is spent on counting the high-q points, which contributes little to the actual data analysis.

5.4. Results

5.4.1. Cyclic voltammogram (CV)

We first determined the electrochemical window, i.e. the voltage range in which the generation of electrolysis products can be ignored. This window is also a qualitative test of the existence of impurities in the RTIL. The CV curve (Figure 5.2) is typical for an RTIL, essentially flat at low voltages and increasing sharply when the potential becomes either too high or too low. If the threshold current density is chosen to be $0.025 mA/cm^2$ (which is below the thresholds commonly used[**74, 75**], $0.1-1.0 mA/cm^2$) the cathode and

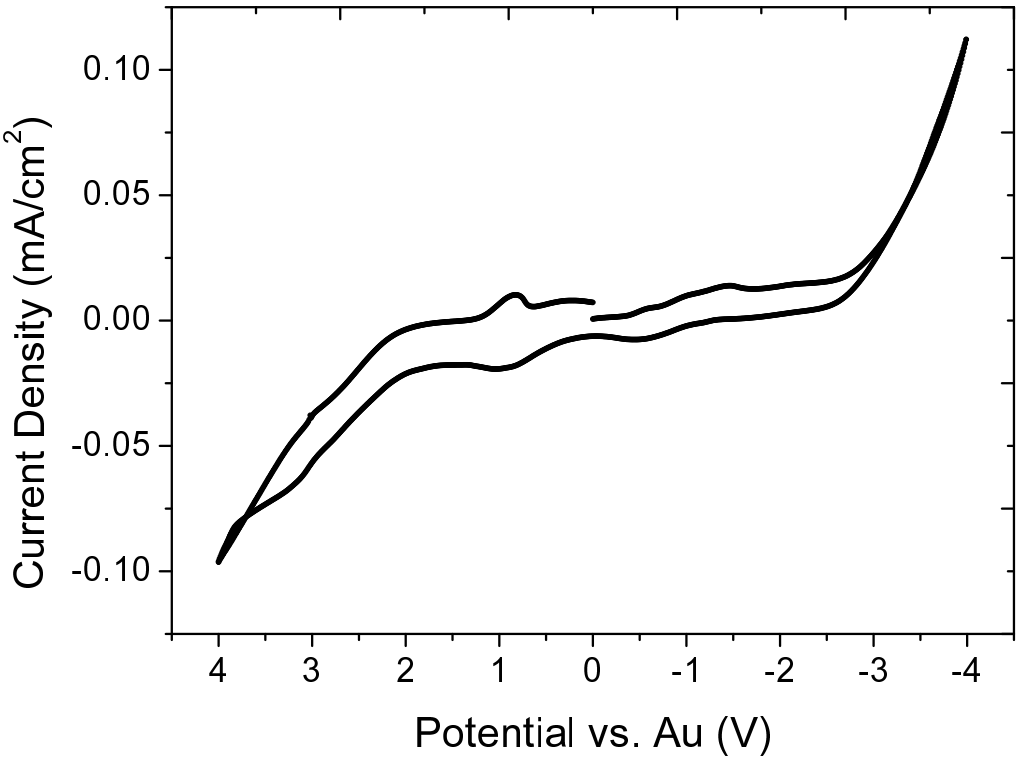

Figure 5.2. Cyclic voltammogram for [MTOA] $^{+}$ [NTF_2] $^{-}$ recorded at sweep rate 10mV/s. The potential was measured against the Au wire pseudo-reference electrode (see Figure 5.1)

anode limit are -3.2V and +2.4V respectively, or 5.6V for the width of the electrochemical window. This is roughly in agreement with number reported by Ueda and coworkers in their study of the same RTIL[**76**]. The potential range during our experiment was -2.20V to +2.35V, i.e. within the electrochemical window.

5.4.2. Time dependent structure of the crowding layer for an increment in potential.

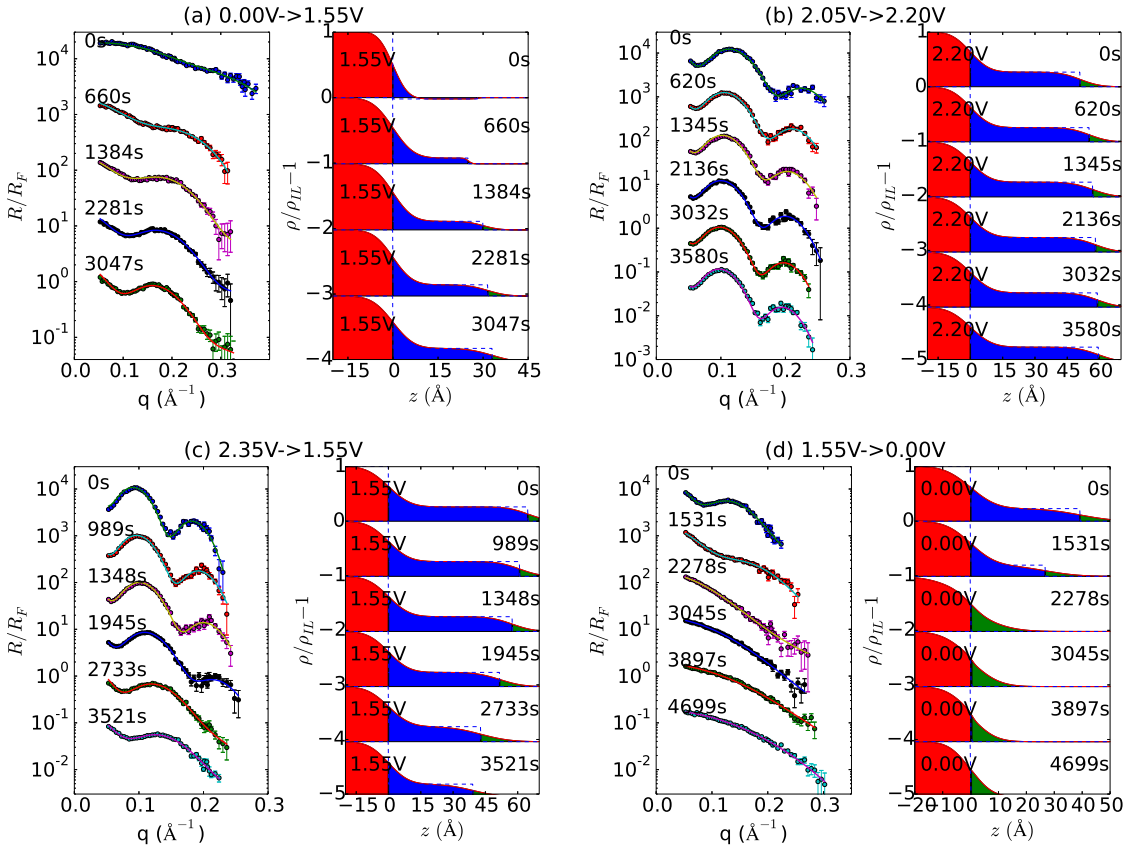

Figure 5.3. In each of the three data sets (a)-(d), the left panels show reflectivity data (solid dots) at different times and best fits with one-slab model (lines through data). The right panels are the normalized electron density profiles corresponding to the best fit. The labels at top give the change of voltage after which the time-dependent data were collected.

When a high potential is applied, the anions will come close to the surface and form a crowding layer. This process requires the reorganization of anions/cations up to several layers on the surface. We previously reported that the data were stable after 20mins for $[TDTHP]^+[NTF_2]^-$, but the time dependence was not studied in detail at the time. We have now recorded the XRR data at various stages during the formation of the crowded layer: these are shown in Figure 5.3. Each XRR measurement takes about 5mins, thus fast dynamics is not captured. The XRR for the initial state at V=0 is featureless in

the observable momentum transfer range (0-0.3Å^{-1}), meaning that there is no observable structure normal to the interface within the liquid near the interface. When a voltage of 1.55V is applied (Figure 5.3 (a)), An oscillating pattern in the reflectivity develops at t=660s, increases in amplitude and shifts towards lower q at t = 1384s. This indicates that a layer at the interface is growing in thickness. The XRR patterns at t=2281s and t=3041s are almost identical, indicating the formation of the crowded layer has been completed.

It worth mentioning that the XRR data are convolved with time, as the interfacial structures keep changing during scans. However, the fitting of XRR data is very sensitive to the peaks and dips in the XRR data, thus the time resolution is actually less than the XRR scan time. In this study, only the order of magnitude is estimated rather than the precise time.

This oscillation in the reflectivity curve is due to the formation of a crowded layer on the surface of silicon, in which anions, which have higher electron density, are enriched and create the electron density contrast seen by X-rays. The simplest model for fitting this pattern is a one-slab model in which we assume that the interfacial layer is uniform, with electron density ρ and thickness W, while the silicon substrate and bulk RTIL are modeled as semi-infinite media with constant electron density. Fitting the data with this model (Figure 5.3 a) shows the interfacial layer increases from 25Å at T=660s to 33Å at T=3047s.

The time dependence of W can be fitted with an exponential decay function, $W(t) = W_0 - A\exp(-t/\tau)$. However, the initial value, $W(t = 0)$, is below the resolution limit (as represented by the large error bar in Figure 5.1 (a). $W(0) = 0$Å if the RTIL near

the surface is no different from the bulk liquid at t=0. On the other hand, perhaps $W(0) \sim 10$Å if a monolayer of anions (too thin to be seen given the range of our reflectivity scans) has formed on the silicon surface even before the voltage is applied. In Figure 5.4 (a), fitting using the two extreme cases yields time constant τ of 448s for $W(0) = 0$Å and 614s for $W(0) = 10$Å. These numbers, while different, are of the same order of magnitude, the significance of which will be discussed below. The electron density enhancement above the bulk liquid electron density stays around 25% for all time steps. In fact, the density enhancement is the same even at higher potentials (5.1 (b)-(c)), suggesting that this is the saturated density of the crowding layer.

Time dependent XRR with a much smaller potential increment, a change from 2.05V to 2.20V, shows similar behavior. The stabilized interfacial layer width at 2.05V was obtained as before by repeating the XRR scan multiple times until the data stopped changing. It takes 620s to add 4Å and another 3000s to add another 4Å. The fitting yields a somewhat longer time constant, $\tau = 1128$s.

5.4.3. Time dependent structure of the crowding layer for a decrement in potential.

To exclude the possibility that the interfacial layer is just an irreversible electrolysis product that develops with time, XRR measurements were performed when the potential was decreased from 2.35V to 1.55V, shown in Figure 5.3 (c). The reflectivity oscillation pattern shifts towards higher q, indicating thinning of the crowding layer with time. The $D - t$ relationship can be fitted with an exponentially decaying function, which gives us

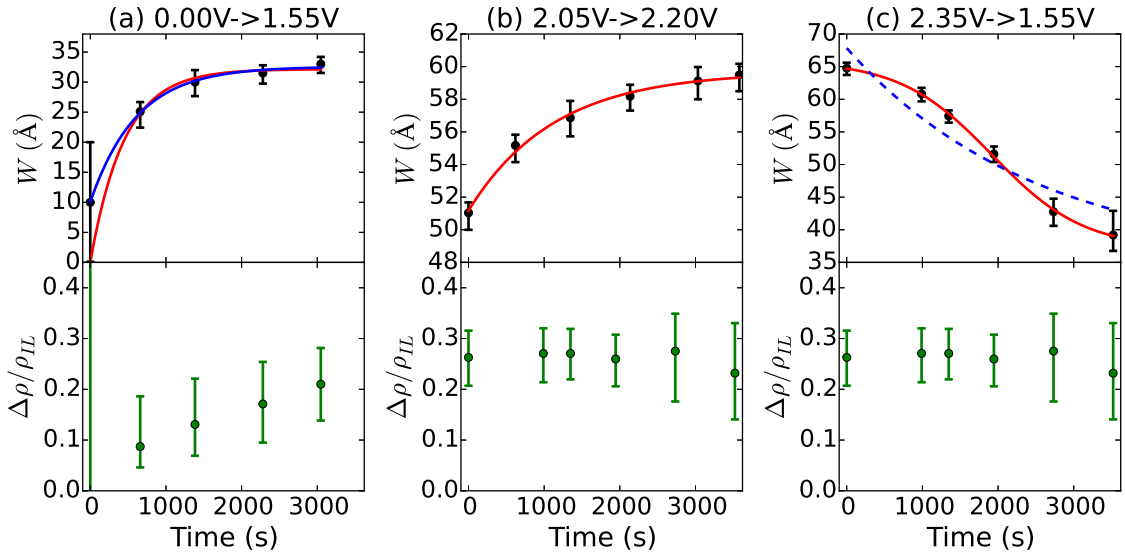

Figure 5.4. Fitting parameters of the interfacial layer as functions of time, for the three cases in Figure 5.3 (a)-(c). Upper graphs show layer width; lower graphs show electron density enhancement above the bulk RTIL electron density. The width data are fitted with exponential decay functions or other functions as described in the text.

a time constant of 2500 sec. However, as shown in Figure. 5.4 (c), it is much better fitted[**77**] with

$$W(t) = \frac{A - B}{1 + \exp[(t - t_0)/\tau]} + B \tag{5.5}$$

The best fit parameters are $A = 66$Å, $B = 37$Å, $t_0 = 1917$s, $\tau = 609$s. The fact that the logistic function fits better than an exponential function suggests that the decrement and increment in potential, corresponding to the thinning and thickening of the crowding layer respectively, possess different kinetics. For example, thinning may require the anions to detach from the crowding layer first. The B value of 37Å is 4Å higher than the previous W value of 33Å at the same voltage, a sign that the crowding layer doesn't fully recover to its initial width. The differential form is a good way to better assess the validity of the

logistic function,

$$\frac{dW(t)}{dt} = \frac{-1}{\tau}\frac{[W(t)-B][A-W(t)]}{A-B}, \qquad W(t=-\infty) = A \tag{5.6}$$

A, B are the initial and final width. The $[W(t)-B]$ term stands for the difference from equilibrium, while $[A-W(t)]$ stands for the "local field" the persists in the crowding layer even after the applied potential has been changed.

The fringes on the XRR data weaken and disappeared after the voltage was set to from 1.55V to 0.00V. Unfortunately, not enough XRR scans were taken during this period. Nevertheless, the time for this dissipation process has the same order of magnitude as the time scales obtained by fitting. In addition, the dissipation at zero voltage demonstrates that the crowding layer isn't due to oxidation of substrate or electrolysis, but is due to the aggregation of anions.

5.5. Discussion

There is no generally accepted theory of the ion dynamics in an RTIL, but as noted earlier, there are several theoretical predictions. Bazant et al.[**66**] describe various different characteristic times associated with double layer charging in electrochemical systems. In the following, l_D is the Debye length, L is the size of the electrochemical cell (distance between anode and cathode) and D is the diffusion constant. Two obvious timescales are $\tau_D = l_D^2/D$ and $\tau_L = L^2/D$. These are the time constants associated with diffusion over very different length scales: τ_L is the time constant for diffusion across the macroscopic length of the cell, whereas τ_D is associated with local charge redistribution. Bazant et

al[**66**] argue that the harmonic mean $\tau_c = l_D L/D$, in other words RC, is the primary timescale for diffuse-charge dynamics in electrochemical cells.

Order-of-magnitude estimates are instructive. For a typical RTIL system, $l_D \sim 1$Å, and $D \sim 10^2 \mu m^2 s^{-1}$. Taking $L = 3mm$, we get $\tau_c \sim 3$ ms and $\tau_L \sim 9 \times 10^4$s. Of course τ_D is far smaller. Comparing to our own results, the differences in the time scales observed in different measurements, or the differences resulting from different fitting assumptions, are small in relation to the order-of-magnitude inconsistency: τ_c and τ_D are far too small, while τ_L is too large.

Zhao [**68**] proposed instead a time constant $\tau_c' = \tau_c \sqrt{l_D/l_c} = l_D^{3/2} L/D\sqrt{l_c}$, where l_c is the typical length of charge correlations. Setting l_c to be the size of anion/cation of RTIL (~ 10Å), this would mean $\tau_c' \sim 1ms$, also inconsistent with our results. If l_c is larger, the timescale is even smaller.

Lee et al.[**67**] have developed a lattice liquid model for ionic liquids, and used it to perform 'numerical experiments' yielding interface charge vs time. They see a rapid initial rise in the interface charge, followed by a slow decay. The rapid rise would not be visible to our measurements, but the slow decay does not agree with our observations; we see a slow rise. Curiously, however, the simulations when performed for different l_c and l_D are consistent with a decay time constant

$$\tau_L' = \tau_L (l_D/l_c)^{3/2} = L^2/D(l_D/l_c)^{3/2} \tag{5.7}$$

The qualitative physics of such a time scale is not clear; this expression follows only from the scaling behavior of the model results. However, our order-of-magnitude estimates, again taking l_c to be 10 Å, gives us $\tau_L' \sim 2800s$. In other words, with these

estimated numbers, $\tau_D << \tau_c << \tau_c' << \tau_L' << \tau_L$. Of these, τ_L' is closest in order of magnitude to the timescales for charging that we observe. Interestingly, $\tau_L' = \tau_c' \cdot L/l_c$, which seems to suggest that ultra-slow process is made up of L/l_c consequent elementary charging processes.

It worth noting here that whether RTILs are fully dissociated or just weakly dissociated (similar to aqueous solutions) is still under debate[**78, 51, 79, 52**]. The Debye length of RTILs measured by surface force apparatus is about 7nm, almost two orders of magnitude larger than the value assuming full dissociation[**51**]. In this scenario, τ_c will be order of 10ms, while τ_L' is not affected if we assume that l_D/l_c doesn't change. As reported in several studies[**73, 58, 59, 60, 61**], the charge of anion/cation in RTILs are usually less than unit charge (partial charge). However, this effect could only rescale the Debye length by less than one order, which couldn't explain the ultra-slow dynamics we observed.

We can now ask why other experiments discussed in the introduction report various timescales ranging from 1 sec to 100 sec. Of course different materials may have different behavior, but we also suggest that because of the presence of multiple processes with different timescales[**66**], the timescales observed will reflect the timescales of the experiment. In other words, our slower study observes the presence of slower mechanisms, perhaps involving long-length-scale rearrangements, while faster measurements observe the effects of faster rearrangement mechanisms occurring over shorter length scales.

5.6. Conclusion

It is already widely recognized that RTIL behavior is quite complex, and there are a number of anomalous experimental results. For example, the measured RTIL interfacial

capacitance decreases with increasing frequency[**39**]. a result that can also be interpreted as being due to the superposition of multiple dynamic processes with different timescales. An increase in our understanding of these processes, correlating macroscopic measurements such as capacitance with nanoscale characterization, is likely to lead to a better fundamental understanding of the RTIL-electrode interface and potentially to better RTILs and RTIL-based devices.

CHAPTER 6

Future Work and Summary

6.1. Future work

6.1.1. RTILs in solvents, a potential way to verify GC/GCS theory

RTILs are considered as solvent-free salts with high concentration of charge, whose electrochemical properties differ from those of diluted aqueous electrolytes significantly. RTILs can be diluted with non-aqueous electrolytes, such as acetonitrile, tetrahydrofuran, 2-Methyltetrahydrofuran, propylene carbon, dimethyl carbonate etc. The solvents in RTILs have been found to considerably alter the transport properties of the mixtures such as conductivities and conductivities [**80, 81**].

Kornyshev built a lattice model showing that solvent molecules can occupy the lattice next to the electrode leading to anomalies in differential capacitance [**38**]. To be more specific, the differential capacitance changes from bell shape to camel shape when solvents taking $\geq 1/3$ of the lattices. Electrochemical impedance spectroscopy(EIS) and X-ray scattering experiments can be performed on mixture of RTILs and solvents to test those predictions.

Additionally, RTILs-solvent mixtures may throw light on understanding the distribution of ions/particles near charged surface. The widely adopted Gouy-Chapman(GC) / Gouy-Chapman-Stern(GCS) theory is derived from thermodynamic perspective without taking. Numerous X-ray experiments were conducted to attack this problem, with

techniques including X-ray standing wave[**37**], X-ray reflectivity[**82, 83, 84, 85**], small angle X-ray scattering [**86**], X-ray fluorescence[**87**], X-ray photoelectron spectroscopy[**88**]. However, the result from those experiments dont always agree with each other. For example, a non-monotonic ion distribution was reported by Luo[**84**] which cant be explained by GC/GCS theory.

Part of the experimental difficulties are due to the high charge and low electron number carried by a normal ion. For example, the heaviest metal ion is Cs^+, with +1e charge and 54 electrons. Cs^+ can easily compensate a charged surface (a typical charge density is only $10 - 30\mu C/cm^2$) without raising the surface electron density too much, making it hard to be detected with X-ray methods.

The anions/cations in RTILs carry less than unit charge, due to the partial charge effect. Additionally, through molecular engineering, the electron density of RTILs can be improved by replacing the light atoms with heavy atoms (e.g. replacing oxygen with sulfur). Its even possible to introduce atoms with appropriate absorption edges to RTILs for resonant X-ray studies. Thus, RTILs-solvent mixtures have the potential to improve current X-ray studies aiming at the direct verification of the GC/GCS theory.

6.2. Summary

The ability to retrieve information from XRR data is tested by numerical experiments with artificial data. By isolating the parameters, the effects of slab width, electron density contrast and maximal wave transfer are studied individually. It's demonstrated that best-fit/global minima, result reported by most XRR studies, don't necessary reflect the real EDP. By contrast, mapping the merit function in the parametric space can capture

much more details. Additionally, the widely accepted concepts such as theoretical spatial resolution (π/q_{max}) and Patterson function will fail in many cases where the contrast of EDP is too low or the scan range isn't enough.

The interface between hydrophobic OTS film and several solvents is studied with XRR in a transmission-cell setup. The solvents, from water, acetone, to alcohol (methanol, ethanol, 1-propanol), to alkane (pentane, hexane and heptane), vary significantly in terms of polarity and hydrogen bonding. However, the XRR data from different solvents are subtle. The contour mapping technique elicited earlier is employed to extract information about the solid-liquid interface. Electron density depletion due to methyl terminal of solvent molecules (methyl gap) and due to the reduced surface density compared to the bulk density (density gap) are analyzed. Water, acetone and methanol are found to have a larger gap than ethanol and propanol, while the alkanes don't appear shown gap other than the methyl gap. This difference derives from the polarity/hydrogen bonding that tends to pull the molecules at the hydrophobic surface into the bulk.

XRR technique is employed to study the structures and dynamics of room temperature ionic liquids (RTILs) at an electrified surface. Conductive silicon which has small electron density is used which maximize the EDP contrast. Meantime RTIL with large electrochemical window, high electron density difference between anions and cations, and stable chemical structures against beam damage, is chosen for the experiment. This makes it possible to directly observe the formation of crowding layer. The thickness of this crowding layer is found to be a square-root dependent of the applied voltage with an offset. The square root relation has been predicted without the offset term. This suggests that the formation of crowding layer requires to cross an energy barrier, which may originate

from the Gouy-Chapman layer. More interestingly, the composition of the crowding layer isn't pure anion as predicted by theories, but anion and cation with ratio of 4:1. However, the crowding layer won't possess a reasonable charge density unless the charge carried by anion/cation in RTIL is less than unite charge. The other possible explanation of compression due to electrical attraction is also discussed.

The time scale for the formation and dissipation of crowding layer in RTILs is also studied with XRR. An ultra-slow dynamic which is ranged between 400-1100 seconds is found, five decades longer than the RC constant, but two orders slower than the free diffusion across the cell. The comparison of possible dynamics in RTILs suggests the crowding layer isn't due to local anion/cation redistribution, but due to a collective re-ordering of anion/cation that across the whole electrochemical cell.

The results presented in this thesis exhibit many observations that haven't been predicted previously. They reflect the complex nature of RTILs that may be not considered or oversimplified in theories and simulations. Thus, these findings may benefit both research and applications on RTILs and RTIL based devices.

References

[1] H. Kiessig, "Untersuchungen zur totalreflexion von röntgenstrahlen," *Annalen der Physik*, vol. 402, no. 6, pp. 715–768, 1931.

[2] L. G. Parratt, "Surface studies of solids by total reflection of x-rays," *Physical Review*, vol. 95, no. 2, p. 359, 1954.

[3] O. H. Seeck and B. Murphy, *X-Ray Diffraction: Modern Experimental Techniques*. CRC Press, 2015.

[4] S. M. Danauskas, M. K. Ratajczak, Y. Ishitsuka, J. Gebhardt, D. Schultz, M. Meron, B. Lin, and K. Y. C. Lee, "Monitoring x-ray beam damage on lipid films by an integrated brewster angle microscope/x-ray diffractometer," *Review of Scientific Instruments*, vol. 78, no. 10, p. 103705, 2007.

[5] E. Spiller, "Characterization of multilayer coatings by x-ray reflection," *Revue de Physique Appliquée*, vol. 23, no. 10, pp. 1687–1700, 1988.

[6] A. Nelson, "Co-refinement of multiple-contrast neutron/x-ray reflectivity data using motofit," *Journal of Applied Crystallography*, vol. 39, no. 2, pp. 273–276, 2006.

[7] H. Benaroya, S. M. Han, and M. Nagurka, *Probability Models in Engineering and Science*, vol. 193. CRC Press, 2005.

[8] C.-J. Yu, A. Richter, A. Datta, M. Durbin, and P. Dutta, "Observation of molecular layering in thin liquid films using x-ray reflectivity," *Physical Review Letters*, vol. 82, no. 11, p. 2326, 1999.

[9] J. G. Skellam, "The frequency distribution of the difference between two poisson variates belonging to different populations.," *Journal of the Royal Statistical Society. Series A (General)*, vol. 109, no. Pt 3, pp. 296–296, 1945.

[10] C. F. Laub and T. L. Kuhl, "Fitting a free-form scattering length density profile to reflectivity data using temperature-proportional quenching," *The Journal of Chemical Physics*, vol. 125, no. 24, p. 244702, 2006.

[11] A. Van der Lee, F. Salah, and B. Harzallah, "A comparison of modern data analysis methods for x-ray and neutron specular reflectivity data," *Journal of Applied Crystallography*, vol. 40, no. 5, pp. 820–833, 2007.

[12] E. L. Hanson, J. Schwartz, B. Nickel, N. Koch, and M. F. Danisman, "Bonding self-assembled, compact organophosphonate monolayers to the native oxide surface of silicon," *Journal of the American Chemical Society*, vol. 125, no. 51, pp. 16074–16080, 2003.

[13] E. Chason and T. Mayer, "Thin film and surface characterization by specular x-ray reflectivity," *Critical Reviews in Solid State and Material Sciences*, vol. 22, no. 1, pp. 1–67, 1997.

[14] H. You, C. Melendres, Z. Nagy, V. Maroni, W. Yun, and R. Yonco, "X-ray-reflectivity study of the copper-water interface in a transmission geometry under in situ electrochemical control," *Physical Review B*, vol. 45, no. 19, p. 11288, 1992.

[15] A. L. Patterson, "A direct method for the determination of the components of interatomic distances in crystals," *Zeitschrift für Kristallographie-Crystalline Materials*, vol. 90, no. 1, pp. 517–542, 1935.

[16] G. Evmenenko, T. T. Fister, D. B. Buchholz, Q. Li, K.-S. Chen, J. Wu, V. P. Dravid, M. C. Hersam, P. Fenter, and M. J. Bedzyk, "Morphological evolution of multilayer ni/nio thin film electrodes during lithiation," *ACS Applied Materials & Interfaces*, vol. 8, no. 31, pp. 19979–19986, 2016.

[17] B. Bataillou, H. Moriceau, and F. Rieutord, "Direct inversion of interfacial reflectivity data using the patterson function," *Journal of Applied Crystallography*, vol. 36, no. 6, pp. 1352–1355, 2003.

[18] J. T. Kellis, K. Nyberg, A. R. Fersht, *et al.*, "Contribution of hydrophobic interactions to protein stability," *Nature*, vol. 333, pp. 784–786, JUN 23 1988.

[19] M. Prabaharan and S. Gong, "Novel thiolated carboxymethyl chitosan-g-β-cyclodextrin as mucoadhesive hydrophobic drug delivery carriers," *Carbohydrate Polymers*, vol. 73, no. 1, pp. 117–125, 2008.

[20] C. Tanford, *The Hydrophobic Effect: Formation of Micelles and Biological Membranes 2d Ed.* J. Wiley., 1980.

[21] M. Mezger, H. Reichert, S. Schöder, J. Okasinski, H. Schröder, H. Dosch, D. Palms, J. Ralston, and V. Honkimäki, "High-resolution in situ x-ray study of the hydrophobic gap at the water–octadecyl-trichlorosilane interface," *Proceedings of the National Academy of Sciences*, vol. 103, no. 49, pp. 18401–18404, 2006.

[22] A. Poynor, L. Hong, I. K. Robinson, S. Granick, Z. Zhang, and P. A. Fenter, "How water meets a hydrophobic surface," *Physical Review Letters*, vol. 97, no. 26, p. 266101, 2006.

[23] A. Uysal, M. Chu, B. Stripe, A. Timalsina, S. Chattopadhyay, C. M. Schlepütz, T. J. Marks, and P. Dutta, "What x rays can tell us about the interfacial profile of water near hydrophobic surfaces," *Physical Review B*, vol. 88, no. 3, p. 035431, 2013.

[24] A. Poynor, L. Hong, I. K. Robinson, S. Granick, P. A. Fenter, and Z. Zhang, "Poynor et al. reply," *Physical Review Letters*, vol. 101, no. 3, p. 039602, 2008.

[25] J. Haddad, H.-G. Steinruck, H. Hlaing, S. Kewalramani, D. Pontoni, H. Reichert, B. M. Murphy, S. Festersen, B. Runge, O. M. Magnussen, *et al.*, "Order and melting in self-assembled alkanol monolayers on amorphous sio2," *The Journal of Physical Chemistry C*, vol. 119, no. 31, pp. 17648–17654, 2015.

[26] B. Ocko, X. Wu, E. Sirota, S. Sinha, O. Gang, and M. Deutsch, "Surface freezing in chain molecules: Normal alkanes," *Physical Review E*, vol. 55, no. 3, p. 3164, 1997.

[27] Y. Wang and M. Lieberman, "Growth of ultrasmooth octadecyltrichlorosilane self-assembled monolayers on sio2," *Langmuir*, vol. 19, no. 4, pp. 1159–1167, 2003.

[28] H.-G. Steinruck, J. Will, A. Magerl, and B. M. Ocko, "Structure of n-Alkyltrichlorosilane Monolayers on Si (100)/SiO2," *Langmuir*, vol. 31, no. 43, pp. 11774–11780, 2015.

[29] W. Press, S. Teukolsky, and W. V. B. Flannery, "Numerical recipes in C," 1988.

[30] P. Jiang, S.-Y. Li, H. Sugimura, and O. Takai, "Pattern design in large area using octadecyltrichlorosilane self-assembled monolayers as resist material," *Applied Surface Science*, vol. 252, no. 12, pp. 4230–4235, 2006.

[31] H.-G. Steinruck, A. Schiener, T. Schindler, J. Will, A. Magerl, O. Konovalov, G. Li Destri, O. H. Seeck, M. Mezger, J. Haddad, *et al.*, "Nanoscale structure of si/sio2/organics interfaces," *ACS Nano*, vol. 8, no. 12, pp. 12676–12681, 2014.

[32] P. Walden *et al.*, "Molecular weights and electrical conductivity of several fused salts," *Bull. Acad. Imper. Sci.(St. Petersburg)*, vol. 8, pp. 405–422, 1914.

[33] P. Bonhote, A.-P. Dias, N. Papageorgiou, K. Kalyanasundaram, and M. Grätzel, "Hydrophobic, highly conductive ambient-temperature molten salts," *Inorganic Chemistry*, vol. 35, no. 5, pp. 1168–1178, 1996.

[34] M. J. Earle and K. R. Seddon, "Ionic liquids. green solvents for the future," *Pure and Applied Chemistry*, vol. 72, no. 7, pp. 1391–1398, 2000.

[35] M. V. Fedorov and A. A. Kornyshev, "Ionic liquids at electrified interfaces," *Chemical Reviews*, vol. 114, no. 5, pp. 2978–3036, 2014.

[36] W. Schmickler and E. Santos, *Interfacial Electrochemistry*. Springer Science & Business Media, 2010.

[37] M. J. Bedzyk, G. M. Bommarito, M. Caffrey, and T. L. Penner, "Diffuse-double layer at a membrane-aqueous interface measured with x-ray standing waves," *Science*, vol. 248, no. 4951, pp. 52–56, 1990.

[38] A. A. Kornyshev, "Double-layer in ionic liquids: paradigm change?," *The Journal of Physical Chemistry B*, vol. 111, no. 20, pp. 5545–5557, 2007.

[39] V. Lockett, R. Sedev, J. Ralston, M. Horne, and T. Rodopoulos, "Differential capacitance of the electrical double layer in imidazolium-based ionic liquids: influence of potential, cation size, and temperature," *The Journal of Physical Chemistry C*, vol. 112, no. 19, pp. 7486–7495, 2008.

[40] M. V. Fedorov and A. A. Kornyshev, "Towards understanding the structure and capacitance of electrical double layer in ionic liquids," *Electrochimica Acta*, vol. 53, no. 23, pp. 6835–6840, 2008.

[41] J. Bowers, M. C. Vergara-Gutierrez, and J. R. Webster, "Surface ordering of amphiphilic ionic liquids," *Langmuir*, vol. 20, no. 2, pp. 309–312, 2004.

[42] Y. Lauw, M. D. Horne, T. Rodopoulos, V. Lockett, B. Akgun, W. A. Hamilton, and A. R. Nelson, "Structure of [c4mpyr][ntf2] room-temperature ionic liquid at charged gold interfaces," *Langmuir*, vol. 28, no. 19, pp. 7374–7381, 2012.

[43] M. Mezger, H. Schröder, H. Reichert, S. Schramm, J. S. Okasinski, S. Schöder, V. Honkimäki, M. Deutsch, B. M. Ocko, J. Ralston, *et al.*, "Molecular layering of fluorinated ionic liquids at a charged sapphire (0001) surface," *Science*, vol. 322, no. 5900, pp. 424–428, 2008.

[44] M. Mezger, S. Schramm, H. Schröder, H. Reichert, M. Deutsch, E. J. De Souza, J. S. Okasinski, B. M. Ocko, V. Honkimäki, and H. Dosch, "Layering of [bmim]+-based ionic liquids at a charged sapphire interface," *The Journal of Chemical Physics*, vol. 131, no. 9, p. 094701, 2009.

[45] Z. Brkljaca, M. Klimczak, Z. Milicevic, M. Weisser, N. Taccardi, P. Wasserscheid, D. M. Smith, A. Magerl, and A.-S. Smith, "Complementary molecular dynamics and x-ray reflectivity study of an imidazolium-based ionic liquid at a neutral sapphire interface," *The Journal of Physical Chemistry Letters*, vol. 6, no. 3, pp. 549–555, 2015.

[46] H. Zhou, M. Rouha, G. Feng, S. S. Lee, H. Docherty, P. Fenter, P. T. Cummings, P. F. Fulvio, S. Dai, J. McDonough, *et al.*, "Nanoscale perturbations of room temperature ionic liquid structure at charged and uncharged interfaces," *ACS Nano*, vol. 6, no. 11, pp. 9818–9827, 2012.

[47] A. Uysal, H. Zhou, G. Feng, S. S. Lee, S. Li, P. Fenter, P. T. Cummings, P. F. Fulvio, S. Dai, J. K. McDonough, *et al.*, "Structural origins of potential dependent hysteresis at the electrified graphene/ionic liquid interface," *The Journal of Physical Chemistry C*, vol. 118, no. 1, pp. 569–574, 2013.

[48] R. Yamamoto, H. Morisaki, O. Sakata, H. Shimotani, H. Yuan, Y. Iwasa, T. Kimura, and Y. Wakabayashi, "External electric field dependence of the structure of the electric double layer at an ionic liquid/au interface," *Applied Physics Letters*, vol. 101, no. 5, p. 053122, 2012.

[49] R. Hayes, N. Borisenko, M. K. Tam, P. C. Howlett, F. Endres, and R. Atkin, "Double layer structure of ionic liquids at the au (111) electrode interface: an atomic force microscopy investigation," *The Journal of Physical Chemistry C*, vol. 115, no. 14, pp. 6855–6863, 2011.

[50] J. M. Black, D. Walters, A. Labuda, G. Feng, P. C. Hillesheim, S. Dai, P. T. Cummings, S. V. Kalinin, R. Proksch, and N. Balke, "Bias-dependent molecular-level structure of electrical double layer in ionic liquid on graphite," *Nano Letters*, vol. 13, no. 12, pp. 5954–5960, 2013.

[51] M. A. Gebbie, M. Valtiner, X. Banquy, E. T. Fox, W. A. Henderson, and J. N. Israelachvili, "Ionic liquids behave as dilute electrolyte solutions," *Proceedings of the National Academy of Sciences*, vol. 110, no. 24, pp. 9674–9679, 2013.

[52] M. A. Gebbie, M. Valtiner, X. Banquy, W. A. Henderson, and J. N. Israelachvili, "Reply to perkin et al.: Experimental observations demonstrate that ionic liquids form

both bound (stern) and diffuse electric double layers," *Proceedings of the National Academy of Sciences*, vol. 110, pp. E4122–E4122, 2013.

[53] A. Uysal, H. Zhou, G. Feng, S. S. Lee, S. Li, P. T. Cummings, P. F. Fulvio, S. Dai, J. K. McDonough, Y. Gogotsi, *et al.*, "Interfacial ionic liquids: connecting static and dynamic structures," *Journal of Physics: Condensed Matter*, vol. 27, no. 3, p. 032101, 2014.

[54] P. Fenter and N. C. Sturchio, "Mineral–water interfacial structures revealed by synchrotron x-ray scattering," *Progress in Surface Science*, vol. 77, no. 5, pp. 171–258, 2004.

[55] G. Binnig, H. Rohrer, C. Gerber, and E. Weibel, "7× 7 reconstruction on si (111) resolved in real space," *Physical Leview Letters*, vol. 50, no. 2, p. 120, 1983.

[56] E. Sloutskin, B. M. Ocko, L. Tamam, I. Kuzmenko, T. Gog, and M. Deutsch, "Surface layering in ionic liquids: an x-ray reflectivity study," *Journal of the American Chemical Society*, vol. 127, no. 21, pp. 7796–7804, 2005.

[57] M. Z. Bazant, B. D. Storey, and A. A. Kornyshev, "Double layer in ionic liquids: overscreening versus crowding," *Physical Review Letters*, vol. 106, no. 4, p. 046102, 2011.

[58] J. Schmidt, C. Krekeler, F. Dommert, Y. Zhao, R. Berger, L. D. Site, and C. Holm, "Ionic charge reduction and atomic partial charges from first-principles calculations of 1, 3-dimethylimidazolium chloride," *The Journal of Physical Chemistry B*, vol. 114, no. 18, pp. 6150–6155, 2010.

[59] O. Hollóczki, F. Malberg, T. Welton, and B. Kirchner, "On the origin of ionicity in ionic liquids. ion pairing versus charge transfer," *Physical Chemistry Chemical Physics*, vol. 16, no. 32, pp. 16880–16890, 2014.

[60] M. G. Del Pópolo, R. M. Lynden-Bell, and J. Kohanoff, "Ab initio molecular dynamics simulation of a room temperature ionic liquid," *The Journal of Physical Chemistry B*, vol. 109, no. 12, pp. 5895–5902, 2005.

[61] T. G. Youngs and C. Hardacre, "Application of static charge transfer within an ionic-liquid force field and its effect on structure and dynamics," *ChemPhysChem*, vol. 9, no. 11, pp. 1548–1558, 2008.

[62] P. Simon and Y. Gogotsi, "Materials for electrochemical capacitors," *Nature Materials*, vol. 7, no. 11, pp. 845–854, 2008.

[63] N. V. Plechkova and K. R. Seddon, "Applications of ionic liquids in the chemical industry," *Chemical Society Reviews*, vol. 37, no. 1, pp. 123–150, 2008.

[64] L. Smith and B. Dunn, "Opening the window for aqueous electrolytes," *Science*, vol. 350, no. 6263, pp. 918–918, 2015.

[65] F. B. Sillars, S. I. Fletcher, M. Mirzaeian, and P. J. Hall, "Variation of electrochemical capacitor performance with room temperature ionic liquid electrolyte viscosity and ion size," *Physical Chemistry Chemical Physics*, vol. 14, no. 17, pp. 6094–6100, 2012.

[66] M. Z. Bazant, K. Thornton, and A. Ajdari, "Diffuse-charge dynamics in electrochemical systems," *Physical Review E*, vol. 70, no. 2, p. 021506, 2004.

[67] A. A. Lee, S. Kondrat, D. Vella, and A. Goriely, "Dynamics of ion transport in ionic liquids," *Physical Review Letters*, vol. 115, p. 106101, Sep 2015.

[68] H. Zhao, "Diffuse-charge dynamics of ionic liquids in electrochemical systems," *Physical Review E*, vol. 84, no. 5, p. 051504, 2011.

[69] J. Jiang, D. Cao, D.-e. Jiang, and J. Wu, "Time-dependent density functional theory for ion diffusion in electrochemical systems," *Journal of Physics: Condensed Matter*, vol. 26, no. 28, p. 284102, 2014.

[70] B. Roling, M. Drüschler, and B. Huber, "Slow and fast capacitive process taking place at the ionic liquid/electrode interface," *Faraday Discussions*, vol. 154, pp. 303–311, 2012.

[71] R. Atkin, N. Borisenko, M. Drüschler, F. Endres, R. Hayes, B. Huber, and B. Roling, "Structure and dynamics of the interfacial layer between ionic liquids and electrode materials," *Journal of Molecular Liquids*, vol. 192, pp. 44–54, 2014.

[72] N. Nishi, Y. Hirano, T. Motokawa, and T. Kakiuchi, "Ultraslow relaxation of the structure at the ionic liquid— gold electrode interface to a potential step probed by electrochemical surface plasmon resonance measurements: asymmetry of the relaxation time to the potential-step direction," *Physical Chemistry Chemical Physics*, vol. 15, no. 28, pp. 11615–11619, 2013.

[73] M. Chu, M. Miller, and P. Dutta, "Crowding and anomalous capacitance at an electrode–ionic liquid interface observed using operando x-ray scattering," *ACS Central Science*, vol. 2, no. 3, pp. 175–180, 2016.

[74] E. I. Rogers, B. Sljukic, C. Hardacre, and R. G. Compton, "Electrochemistry in room-temperature ionic liquids: potential windows at mercury electrodes," *Journal of Chemical & Engineering Data*, vol. 54, no. 7, pp. 2049–2053, 2009.

[75] M. Hayyan, F. S. Mjalli, M. A. Hashim, I. M. AlNashef, and T. X. Mei, "Investigating the electrochemical windows of ionic liquids," *Journal of Industrial and Engineering Chemistry*, vol. 19, no. 1, pp. 106–112, 2013.

[76] H. Ueda, K. Nishiyama, and S. Yoshimoto, "Electrochemical behavior of bis (trifluoromethylsulfonyl) imide-based ils at gold single crystal electrodes," *ECS Transactions*, vol. 50, no. 11, pp. 175–179, 2013.

[77] S. H. Strogatz, *Nonlinear Dynamics and Chaos: with Applications to Physics, Biology, Chemistry, and Engineering*. Westview Press, 2014.

[78] H. Weingärtner, "Understanding ionic liquids at the molecular level: facts, problems, and controversies," *Angewandte Chemie International Edition*, vol. 47, no. 4, pp. 654–670, 2008.

[79] S. Perkin, M. Salanne, P. Madden, and R. Lynden-Bell, "Is a stern and diffuse layer model appropriate to ionic liquids at surfaces?," *Proceedings of the National Academy of Sciences*, vol. 110, no. 44, pp. E4121–E4121, 2013.

[80] J. Segalini, B. Daffos, P.-L. Taberna, Y. Gogotsi, and P. Simon, "Qualitative electrochemical impedance spectroscopy study of ion transport into sub-nanometer carbon pores in electrochemical double layer capacitor electrodes," *Electrochimica Acta*, vol. 55, no. 25, pp. 7489–7494, 2010.

[81] J. K. McDonough, A. I. Frolov, V. Presser, J. Niu, C. H. Miller, T. Ubieto, M. V. Fedorov, and Y. Gogotsi, "Influence of the structure of carbon onions on their electrochemical performance in supercapacitor electrodes," *Carbon*, vol. 50, no. 9, pp. 3298–3309, 2012.

[82] W. Bu, D. Vaknin, and A. Travesset, "How accurate is poisson-boltzmann theory for monovalent ions near highly charged interfaces?," *Langmuir*, vol. 22, no. 13, pp. 5673–5681, 2006.

[83] G. Luo, S. Malkova, J. Yoon, D. G. Schultz, B. Lin, M. Meron, I. Benjamin, P. Vanỳsek, and M. L. Schlossman, "Ion distributions near a liquid-liquid interface," *Science*, vol. 311, no. 5758, pp. 216–218, 2006.

[84] G. Luo, W. Bu, M. Mihaylov, I. Kuzmenko, M. L. Schlossman, and L. Soderholm, "X-ray reflectivity reveals a nonmonotonic ion-density profile perpendicular to the

surface of ercl3 aqueous solutions," *The Journal of Physical Chemistry C*, vol. 117, no. 37, pp. 19082–19090, 2013.

[85] N. Laanait, M. Mihaylov, B. Hou, H. Yu, P. Vanỳsek, M. Meron, B. Lin, I. Benjamin, and M. L. Schlossman, "Tuning ion correlations at an electrified soft interface," *Proceedings of the National Academy of Sciences*, vol. 109, no. 50, pp. 20326–20331, 2012.

[86] S. Kewalramani, G. I. Guerrero-García, L. M. Moreau, J. W. Zwanikken, C. A. Mirkin, M. Olvera de la Cruz, and M. J. Bedzyk, "Electrolyte-mediated assembly of charged nanoparticles," *ACS Central Science*, vol. 2, no. 4, pp. 219–224, 2016.

[87] W. Bu and D. Vaknin, "X-ray fluorescence spectroscopy from ions at charged vapor/water interfaces," *Journal of Applied Physics*, vol. 105, no. 8, p. 084911, 2009.

[88] M. Favaro, B. Jeong, P. N. Ross, J. Yano, Z. Hussain, Z. Liu, and E. J. Crumlin, "Unravelling the electrochemical double layer by direct probing of the solid/liquid interface," *Nature Communications*, vol. 7, 2016.